CrossMark

A Mini Survey of Methyl Cyanide toward Extended Green Objects

T. Hung[1,2] , Sheng-Yuan Liu[2] , Yu-Nung Su[2], J. H. He[3,4,5] , Hsu-Tai Lee[2,6], Satoko Takahashi[2,7,8] , and Huei-Ru Chen[9]

[1] Department of Astronomy and Astrophysics, University of California, Santa Cruz, CA 95064, USA; tiarahung@ucsc.edu
[2] Institute of Astronomy and Astrophysics, Academia Sinica, P.O. Box 23-141, Taipei 10617, Taiwan
[3] Yunnan Observatories, Chinese Academy of Sciences, 396 Yangfangwang, Guandu District, Kunming, 650216, People's Republic of China
[4] Chinese Academy of Sciences South America Center for Astronomy, China–Chile Joint Center for Astronomy, Camino El Observatorio #1515, Las Condes, Santiago, Chile
[5] Departamento de Astronomía, Universidad de Chile, Casilla 36-D, Santiago, Chile
[6] National Chung Cheng University, No. 168, Sec. 1, University Road, Minhsiung, Chiayi 62102, Taiwan
[7] NAOJ Chile Observatory, Alonso de Córdova 3788, Oficina 61B, Vitacura, Santiago, Chile
[8] National Astronomical Observatory of Japan, 2-21-1 Osawa, Mitaka, Tokyo 181-8588, Japan
[9] Institute of Astronomy and Department of Physics, National Tsing Hua University, Hsinchu 30013, Taiwan

Abstract

We present results of a survey of methyl cyanide (CH_3CN) $J = 12–11$ toward 56 sources, including 35 Extended Green Objects (EGOs) and 21 nearby *AKARI* counterparts, with the Submillimeter Telescope (SMT) in order to characterize the nature of EGOs. CH_3CN, a tracer of hot core emission, is detected in 19 EGOs ($\sim$54%) and five *AKARI* bright sources ($\sim$24%). By analyzing the observed CH_3CN features, we find an average line width of 6.5 km s^{-1}. For the sources detected with CH_3CN, we derive CH_3CN column densities $\log_{10}(N \, [\mathrm{cm}^{-2}]) = 14–17$ with gas temperatures in the range 40–300 K. The small filling factors (10^{-2}–10^{-4}) may reflect the rather compact CH_3CN emitting regions, which correspond to linear sizes of $\sim$0.01–0.08 pc. We also estimate the virial masses and gas masses of these sources. Our derived gas masses are lower than the virial masses, possibly because CH_3CN traces more energetic motions such as outflows and shocks. Alternatively, we cannot rule out that the virial masses are overestimated due to the presence of unresolved CH_3CN kinetic components, such as the rotation structures observed around the young stellar objects.

Key words: ISM: general – stars: formation – submillimeter: ISM

1. Introduction

The identification of massive young stellar objects (MYSOs) is difficult with direct imaging due to the dense clouds surrounding them in their early evolutionary phases. The fast evolution timescale of MYSOs and the fact that MYSOs have a tendency to form in cluster environments make them elusive to study.

Observational investigations have shown that Extended Green Objects (EGOs), which are selected by diffuse 4.5 μm emission, may be promising candidates for massive protostars that are actively accreting and driving outflows (Cyganowski et al. 2008). The Galactic Legacy Infrared Mid-Plane Survey Extraordinaire (GLIMPSE) has brought to light $\sim$300 EGOs using the *Spitzer* four-channeled (3.6, 4.5, 5.8, and 8.0 μm) Infrared Array Camera (IRAC) (Cyganowski et al. 2008). Sources that are characterized by their diffuse and prominent emission at 4.5 μm are called EGOs because the 4.5 μm band is coded as green in the IRAC three-color composite images. Follow-up investigations of the GLIMPSE II data set have revealed nearly 100 more EGOs, expanding the current sample size to about 400 (Chen et al. 2013).

EGOs are promising signposts of MYSOs for the following reasons. To start, their mid-IR colors occupy the same color–color space as the young protostars in infalling envelopes (Cyganowski et al. 2008). As pointed out by Cyganowski et al. (2008), the majority of EGOs (67%) are found in infrared dark clouds (IRDCs) that are considered to be the sites of massive star formation of the earliest stages, and potentially precursors, of star clusters (Rathborne et al. 2005, 2006, 2007).

Polycyclic aromatic hydrocarbon (PAH) features that dominate the emission in 5.8 and 8.0 μm IRAC filter bands in massive star-forming regions (MSFRs) are absent from the 4.5 μm band (Smith et al. 2006). Therefore, the PAH-free 4.5 μm band often exhibits a distinctive morphology in MSFRs unlike in other IRAC bands. The 4.5 μm morphology predominantly traces shock-excited H_2 lines (Noriega-Crespo et al. 2004; De Buizer & Vacca 2010) and CO ($v = 1$–0) band heads (Reach et al. 2006, Figure 1), making it a good indicator of energetic motions, such as protostellar outflows.

Furthermore, their spatial association with methanol masers suggests that EGOs may be MYSOs with active outflows (Cyganowski et al. 2008, 2009). In a survey of Class I 44 GHz and Class II 6.7 GHz methanol masers, a high association rate ($\geqslant$64%) of EGOs and Class II 6.7 GHz methanol masers has been reported (Cyganowski et al. 2009). Class II 6.7 GHz methanol masers are radiatively pumped and exclusively associated with MYSOs (Minier et al. 2003). The Class I 44 GHz methanol masers, which are likely to originate from molecular outflows (Kurtz et al. 2004), were reported with a detection rate of $\sim$89% toward the EGOs associated with the 6.7 GHz masers. Other millimeter observations suggest similar conclusions that sources with extended 4.5 μm features are associated with molecular outflows or ionized jets (Araya et al. 2007; Shepherd et al. 2007; Qiu et al. 2008).

On the other hand, emission mechanisms other than outflow shocks have been proposed to explain the enhanced 4.5 μm emission. For example, De Buizer & Vacca (2010) suggested that both the extinction effect and an exaggeration in color stretch in the 4.5 μm band while producing the IRAC three-color composite image could cause the image to be artificially green. Detailed observational investigation showed that part of the extended 4.5 μm emission can be attributed to light scattering by outflow cavities of embedded MYSOs (Qiu et al. 2008; Lee et al. 2012; Takami et al. 2012). This interpretation, nevertheless, also

employs outflow phenomenon associated with MYSOs. Lee et al. (2012), for example, did detect H_2 outflows toward 12 out of 34 EGOs in their sample, even though the H_2 emission is in general more extended than the 4.5 μm feature. In supernova remnants, the H_2 emission may dominate in all IRAC bands since line emission is the main cooling mechanism in shocked molecular gas (Reach et al. 2006).

Further characterizing the nature of EGOs and their implications is crucial to understanding the early phase of massive star formation. Rotational spectroscopy of methyl cyanide (CH_3CN) is well suited for the purpose of detailing the physical properties of EGOs. Owing to its favorable excitation conditions, CH_3CN has been used to study warm (>100 K) and dense ($>10^5$ cm^{-3}) regions (Purcell et al. 2006) and is an excellent tool for probing the temperatures and column densities in hot molecular cores (HMCs) (Araya et al. 2005, and reference therein). The symmetric-top molecule has a high dipole moment of 3.91 Debye (Boucher et al. 1980) and its rotational energy levels can be characterized by two quantum numbers: J, the total angular momentum, and K, the projection of J along the axis of symmetry (Loren & Mundy 1984). As radiative transitions between K ladders are forbidden, the relative population of its transitions is therefore exclusively determined by collisions. Under the conditions of local thermodynamical equilibrium (LTE), the energy levels of the K components for a given transition from J to $J - 1$ are populated according to the Boltzmann distribution, from which the kinetic temperature can be inferred. The closely spaced K components have the advantage of minimizing relative calibration errors in line intensities, since multiple K components can be covered by a single bandpass.

In addition, CH_3CN also traces gas kinematic structures. Given that EGOs are likely MYSOs associated with active outflows, they are also likely to have circumstellar disks. In some previous studies, CH_3CN has appeared as elongated structures with a velocity gradient perpendicular to the bipolar outflows depicted in CO and HCO^+. One interpretation is that CH_3CN is tracing the rotating tori or disks around the central young stellar object (Johnston et al. 2015; Chen et al. 2016; Beltrán & de Wit 2016, and references therein). Therefore, CH_3CN detection may make it feasible to look for possible disks through high-angular-resolution interferometric imaging in a larger sample.

This paper describes the results from a mini survey of CH_3CN toward a sample of 56 targets, comprising 35 EGOs and 21 AKARI bright sources with moderate separations from the selected EGOs. We outline the source selection criteria and the observation details in Section 2 and describe the spectral data reduction and profile fitting analysis in Section 3. We report our results for the physical parameters derived from the CH_3CN $J = 12$–11 K transitions in Section 4. The implications are discussed in Section 5 and we summarize our work in Section 6.

2. Sample Selection and Observations

2.1. Sample Selection

For our survey, we selected 35 EGOs from the EGO sample of He et al. (2012) with detection of CH_3OH, which is indicative of hot core emissions (van Dishoeck & Blake 1998). The EGO sample studied by He et al. (2012) includes 89 targets that were selected from an EGO catalog compiled by Cyganowski et al. (2008) based on accessibility (decl. $> -38°$) to the Submillimeter Telescope (SMT).

Fourteen of our EGO targets overlap with the near-IR survey sample in Lee et al. (2012). Among these sources, six EGOs (G11.92–0.61, G16.59–0.05, G19.01–0.03, G19.88–0.53, G35.13–0.74, and G35.79–0.17) are associated with H_2 outflows identified by Lee et al. (2012). In particular, G19.88–0.53 has an H_2 morphology that is consistent with the 4.5 μm emission.

Although EGOs are likely associated with outflow activities, they may not directly coincide with the power source of the outflow. In order to study these potential outflow-driving sources, we also cross-matched the bright source catalog released by the AKARI all-sky survey (Oyabu et al. 2010) and selected 21 sources with notable, but not too distant, offsets ($\sim 15''$–60$''$) from our selected EGOs. The AKARI Infrared Astronomical Satellite was launched in 2006 to carry out an all-sky survey in the mid-IR (9 and 18 μm) and far-IR (50–180 μm). Its sensitivity is higher than that of the Infrared Astronomical Satellite (IRAS) by an order of magnitude. AKARI has a spatial resolution of $30''$–40$''$ in the far-IR bands (Doi et al. 2009). The 5σ detection limit for a point source is estimated to be 50 mJy, 120 mJy, 2.4 Jy, 0.55 Jy, 1.4 Jy, and 6.3 Jy for the 9 μm, 18 μm, 65 μm, 90 μm, 140 μm, and 160 μm bands, respectively. The small angular separation in the sky suggests that the EGOs and their AKARI counterparts are possibly in proximity and physically connected to each other. A full list of the sample targets is presented in Tables 1 and 2.

We detail the properties of our EGO sample and known associations with tracers of massive star formation in Table 1. More than half ($\sim 60\%$) of the EGOs are located within IRDCs, and around 69% of our EGOs are associated with 6.7 GHz Class II CH_3OH masers, suggesting that a majority of the EGOs in our sample are at an early evolutionary stage of massive star formation (Ellingsen 2006). Almost all of our EGOs are associated with the tracer of warm dense gas, $H^{13}CO^+$(3–2). SiO(6–5), an outflow tracer, is detected in the majority (74%) of our EGO sample, while only 34% of the EGOs in our sample display blue asymmetric HCO^+ profiles that indicate infalling gas motion.

2.2. Observations

The observations of CH_3CN were made with the SMT on Mountain Graham near Safford, Arizona, operated by the Arizona Radio Observatory. The observations were carried out between 2010 November and 2011 April. The observing sessions employed the beam-switching (BS) mode with a beam throw of $2'$. Pointing was checked with Saturn at the beginning of each observing session, and the absolute pointing accuracy is estimated to be $2''$ (rms). The ALMA Band 6 sideband-separating receiver was employed to observe the $J = 12$–11 transitions of CH_3CN listed in Table 3. The acousto-optical spectrometer (AOS) of 1024 channels with a 1 MHz spectral resolution (~ 1.36 km s^{-1} at 220.7 GHz) was used. The frequency coverage was 1 GHz centered at 220.7 GHz. The average beam efficiency at 220.7 GHz is ~ 0.75. The main beam size is $\sim 34''$, corresponding to a linear spatial coverage of 0.66 pc at a representative distance of 4 kpc. Apart from the CH_3CN $J = 12$–11 lines, multiple transitions of $CH_3^{13}CN$ $J = 12$–11, ^{13}CO $J = 2$–1, and HNCO are also covered in the bandpass. The data reduction, including spectra summation, averaging, and baseline subtraction, was carried out in CLASS, which is a sub-package of the GILDAS software.[9] For an on-source integration time of ~ 4 to 10

_____

[9] Website: http://www.iram.fr/IRAMFR/GILDAS.

Table 1
Observational Parameters of EGOs

| Object | Position | | $V_{LSR}(\sigma)$[a] (km s^{-1}) | Distance[a] (kpc) | Properties[b] | | | | | | AKARI[c] |
	R.A.(2000)	Decl.(2000)			H^{13}CO$^+$	SiO	HCO$^+$	IRDC	6.7 GHz	CH$_3$OH	
G10.29–0.13	18^{h}08^{m}49^{s}3	−20°05′57″	13.3 ± 0.2	2.1$^{+0.7}_{-0.9}$	y	n	N	y	y	n	
G10.34–0.14	18^{h}09^{m}00^{s}0	−20°03′35″	12.3 ± 0.1	2.0$^{+0.7}_{-1.0}$	y	y	R	y	y	y	
G11.92–0.61	18^{h}13^{m}58^{s}1	−18°54′17″	35.9 ± 0.1	3.7$^{+0.4}_{-0.5}$	y	y	R	y	y	y	1814004−185335
G12.42+0.50	18^{h}10^{m}51^{s}1	−17°55′50″	17.8 ± 0.1	2.3$^{+0.6}_{-0.7}$	y	y	B	n	⋯	y	
G12.68–0.18	18^{h}13^{m}54^{s}7	−18°01′47″	55.5 ± 0.1	4.6$^{+0.3}_{-0.3}$	y	y	⋯	n	y	y	
G14.63–0.58	18^{h}19^{m}15^{s}4	−16°30′07″	18.3 ± 0.1	2.1$^{+0.6}_{-0.7}$	y	y	R	y	⋯	y	
G16.59–0.05	18^{h}21^{m}09^{s}1	−14°31′48″	59.5 ± 0.1	4.3$^{+0.3}_{-0.3}$	y	y	B	y	y	y	1821090−143210
G18.67+0.03	18^{h}24^{m}53^{s}7	−12°39′20″	80.0 ± 0.3	11.0$^{+0.3}_{-0.2}$	y	n	N	n	y	n	1824529−123936
G18.89–0.47	18^{h}27^{m}07^{s}9	−12°41′36″	66.2 ± 0.1	4.4$^{+0.3}_{-0.3}$	y	y	N	y	y	y	1827046−124145
G19.01–0.03	18^{h}25^{m}44^{s}8	−12°22′46″	59.8 ± 0.1	4.1$^{+0.3}_{-0.3}$	y	y	N	y	y	y	
G19.36–0.03	18^{h}26^{m}25^{s}8	−12°03′57″	26.7 ± 0.1	2.4$^{+0.4}_{-0.5}$	y	y	R	y	y	y	
G19.88–0.53	18^{h}29^{m}14^{s}7	−11°50′23″	43.7 ± 0.1	3.3$^{+0.3}_{-0.4}$	y	y	N	y	⋯	y	
G22.04+0.22	18^{h}30^{m}34^{s}7	−09°34′47″	51.2 ± 0.1	3.5$^{+0.3}_{-0.3}$	y	y	R	y	y	y	1830344−093506
G23.01–0.41	18^{h}34^{m}40^{s}2	−09°00′38″	77.5 ± 0.1	4.6$^{+0.3}_{-0.3}$	y	y	B	n	y	y	1834400−090056
G23.96–0.11	18^{h}35^{m}22^{s}3	−08°01′28″	72.1 ± 0.1	4.3$^{+0.3}_{-0.3}$	y	y	⋯	n	y	y	
G24.00–0.10	18^{h}35^{m}23^{s}5	−07°59′32″	70.6 ± 0.2	4.3$^{+0.3}_{-0.3}$	y	n	B	y	y	y	1835231−080003
G24.33+0.14	18^{h}35^{m}08^{s}1	−07°35′04″	113.8 ± 0.1	5.9$^{+0.3}_{-0.3}$	y	y	⋯	y	y	y	
G24.94+0.07	18^{h}36^{m}31^{s}5	−07°04′16″	41.3 ± 0.2	2.9$^{+0.4}_{-0.4}$	y	n	N	n	y	n	1836281−070448
G25.27–0.43	18^{h}38^{m}57^{s}0	−07°00′48″	59.1 ± 0.1	3.8$^{+0.3}_{-0.3}$	⋯	⋯	⋯	y	y	n	1838574−070121
G25.38–0.15	18^{h}38^{m}08^{s}1	−06°46′53″	95.1 ± 0.1	5.2$^{+0.3}_{-0.3}$	y	y	B	y	⋯	y	
G28.28–0.36	18^{h}44^{m}13^{s}2	−04°18′04″	49.1 ± 0.2	3.2$^{+0.3}_{-0.3}$	y	n	B	n	y	y	1844151−041755
G28.83–0.25	18^{h}44^{m}51^{s}3	−03°45′48″	87.3 ± 0.1	4.9$^{+0.3}_{-0.3}$	y	n	R	y	y	n	1844509−034518
G34.26+0.15	18^{h}53^{m}16^{s}4	+01°15′07″	58.9 ± 0.1	3.6$^{+0.4}_{-0.4}$	y	y	B	n	⋯	y	1853192+011447
G34.39+0.22	18^{h}53^{m}19^{s}0	+01°24′08″	57.5 ± 0.1	3.6$^{+0.4}_{-0.4}$	y	y	B	y	⋯	n	1853186+012504
G35.03+0.35	18^{h}54^{m}00^{s}5	+02°01′18″	53.1 ± 0.1	3.4$^{+0.4}_{-0.4}$	y	y	R	n	y	y	
G35.13–0.74	18^{h}58^{m}06^{s}4	+01°37′01″	34.2 ± 0.1	2.3$^{+0.4}_{-0.4}$	y	y	N	n	⋯	y	1858100+013651
G35.79–0.17	18^{h}57^{m}16^{s}7	+02°27′56″	61.5 ± 0.2	3.8$^{+0.4}_{-0.4}$	y	y	⋯	y	y	y	1857164+022819
G37.48–0.10	19^{h}00^{m}07^{s}0	+03°59′53″	58.9 ± 0.2	3.7$^{+0.4}_{-0.4}$	y	n	N	n	y	n	1900060+035941
G39.10+0.49	19^{h}00^{m}58^{s}1	+05°42′44″	23.1 ± 0.2	11.3$^{+0.4}_{-0.4}$	y	y	B	n	y	n	1900575+054308
G40.28–0.22	19^{h}05^{m}41^{s}3	+06°26′13″	73.5 ± 0.1	5.0$^{+0.6}_{-0.6}$	y	y	R	y	⋯	y	1905406+062625
G45.47+0.05	19^{h}14^{m}25^{s}6	+11°09′28″	62.8 ± 0.1	5.9$^{+1.7}_{-1.7}$	y	y	N	y	y	y	1914220+110908
G49.27–0.34	19^{h}23^{m}06^{s}7	+14°20′13″	66.0 ± 0.1	5.5$^{+1.6}_{-1.6}$	y	y	N	y	n	n	
G49.42+0.33	19^{h}20^{m}59^{s}1	+14°46′53″	−20.8 ± 0.3	12.2$^{+0.6}_{-0.5}$	y	n	B	n	y	n	1920574+144633
G58.78+0.64	19^{h}38^{m}49^{s}6	+23°08′40″	32.6 ± 0.1	4.4$^{+1.8}_{-1.8}$	y	y	B	n	⋯	n	
G59.79+0.63	19^{h}41^{m}03^{s}1	+24°01′15″	34.0 ± 0.1	4.2$^{+1.8}_{-1.8}$	y	y	B	y	⋯	y	1941036+240100

Notes.
[a] The systemic velocity V_{LSR} and the kinematic distances for our sample are derived in He et al. (2012). For V_{LSR}, the uncertainties are presented following the ± sign. He et al. (2012) derived V_{LSR} by averaging over several molecular lines.
[b] Association with H^{13}CO$^+$ (3–2): "y" is yes; "n" is no (He et al. 2012); association with SiO(6–5) (He et al. 2012); HCO$^+$ line profile: "B" is a blue HCO$^+$ (1–0) profile; "R" is a red HCO$^+$ (1–0) profile; "N" is a non-asymmetric HCO$^+$ (1–0) profile (Chen et al. 2010); association with infrared dark clouds (Cyganowski et al. 2008); association with 6.7 GHz class II CH$_3$OH maser (Cyganowski et al. 2009); association with CH$_3$OH lines (Ge et al. 2014).
[c] The associated AKARI counterpart.

minutes, this results in a typical noise level of ∼10 mK in the observed spectra, with the typical system temperature being around 200 K.

3. Data Analysis

While analyzing the observed spectra, we first performed Gaussian fitting to all individual spectral features to identify the presence of CH$_3$CN and extract the systemic velocities and line widths for targets that were detected with CH$_3$CN. As listed in Table 3, the observation bandpass covers multiple K components ($K = 0$–9) of the CH$_3$CN $J = 12$–11 transition. We assume the same LSR velocity and the same line width for all the K components but allow the peak line intensity of individual components to vary independently. By carefully checking the line frequencies covered by the bandpass, we also notice and fit the CH$_3^{13}$CN and HNCO 10(1, 9)–9(1, 8) lines simultaneously with Gaussian line profiles that have the same LSR velocity and line width as the CH$_3$CN lines. Given that the CH$_3$CN $K = 0$ and $K = 1$ transitions are closely spaced and generally blended, we define CH$_3$CN detection as having the sum of line intensities of the $K = 0$ and $K = 1$ components exceeding 3σ. Sources with CH$_3$CN $K = 0$ and $K = 1$ intensities in the range 2.5σ–3σ are classified as marginal.

Since the relative population of the CH$_3$CN K-ladder is determined exclusively by collisions, measurements of multiple

Table 2
Observational Parameters of *AKARI* Sources

Object[a]	R.A.(2000)	Decl.(2000)	$V_{\rm LSR}(\sigma)$ (km s^{-1})[b]	*AKARI*
G11.92–AK	$18^{\rm h}14^{\rm m}00\overset{s}{.}4$	$-18°53'35''$	35.88(06)	1814004−185335
G16.59–AK	$18^{\rm h}21^{\rm m}09\overset{s}{.}0$	$-14°32'10''$	59.54(05)	1821090−143210
G18.67–AK	$18^{\rm h}24^{\rm m}52\overset{s}{.}9$	$-12°39'36''$	80.04(28)	1824529−123936
G18.89–AK	$18^{\rm h}27^{\rm m}04\overset{s}{.}6$	$-12°41'45''$	66.21(07)	1827046−124145
G22.04–AK	$18^{\rm h}30^{\rm m}34\overset{s}{.}4$	$-09°35'06''$	51.16(05)	1830344−093506
G23.01–AK	$18^{\rm h}34^{\rm m}40\overset{s}{.}0$	$-09°00'56''$	77.45(05)	1834400−090056
G24.00–AK	$18^{\rm h}35^{\rm m}23\overset{s}{.}1$	$-08°00'03''$	70.61(16)	1835231−080003
G24.94–AK	$18^{\rm h}36^{\rm m}28\overset{s}{.}1$	$-07°04'48''$	41.25(16)	1836281−070448
G25.27–AK	$18^{\rm h}38^{\rm m}57\overset{s}{.}4$	$-07°01'21''$	59.14(03)	1838574−070121
G28.28–AK	$18^{\rm h}44^{\rm m}15\overset{s}{.}1$	$-04°17'55''$	49.07(24)	1844151−041755
G28.83–AK	$18^{\rm h}44^{\rm m}50\overset{s}{.}9$	$-03°45'18''$	87.31(12)	1844509−034518
G34.26–AK	$18^{\rm h}53^{\rm m}19\overset{s}{.}2$	$+01°14'47''$	58.88(03)	1853192+011447
G34.39–AK	$18^{\rm h}53^{\rm m}18\overset{s}{.}6$	$+01°25'04''$	57.46(05)	1853186+012504
G35.13–AK	$18^{\rm h}58^{\rm m}10\overset{s}{.}0$	$+01°36'51''$	34.20(04)	1858100+013651
G35.79–AK	$18^{\rm h}57^{\rm m}16\overset{s}{.}4$	$+02°28'19''$	61.54(13)	1857164+022819
G37.48–AK	$19^{\rm h}00^{\rm m}06\overset{s}{.}0$	$+03°59'41''$	58.93(20)	1900060+035941
G39.10–AK	$19^{\rm h}00^{\rm m}57\overset{s}{.}5$	$+05°43'08''$	23.10(23)	1900575+054308
G40.28–AK	$19^{\rm h}05^{\rm m}40\overset{s}{.}6$	$+06°26'25''$	73.52(04)	1905406+062625
G45.47–AK	$19^{\rm h}14^{\rm m}22\overset{s}{.}0$	$+11°09'08''$	62.81(05)	1914220+110908
G49.42–AK	$19^{\rm h}20^{\rm m}57\overset{s}{.}4$	$+14°46'33''$	−20.76(30)	1920574+144633
G59.79–AK	$19^{\rm h}41^{\rm m}03\overset{s}{.}6$	$+24°01'00''$	33.97(12)	1941036+240100

Notes.
[a] The *AKARI* sources are named after their associated EGO counterparts for convenience. For example, G11.92–AK is close to the EGO G11.92–0.61 in the sky and so on.
[b] $V_{\rm LSR}$ is assumed the same as its EGO counterpart.

Table 3
Spectral Parameters of Observed Molecules

Species	Transition		Rest Frequency (GHz)	A_{ul}[a] (10^{-4} s^{-1})	$E_{\rm upper}$[b] (K)	g_u[c]
CH$_3$CN	$J = 12$–11	$K = 0$	220.74726	9.202	68.87	12.5
		$K = 1$	220.74301	9.138	76.01	12.5
		$K = 2$	220.73026	8.945	97.44	12.5
		$K = 3$	220.70902	8.623	133.16	25
		$K = 4$	220.67929	8.172	183.15	12.5
		$K = 5$	220.64109	7.594	247.40	12.5
		$K = 6$	220.59443	6.887	325.90	25
		$K = 7$	220.53933	6.054	418.63	12.5
		$K = 8$	220.47582	5.094	525.57	12.5
CH$_3^{13}$CN	$J = 12$–11	$K = 0$	220.63807	9.189	68.83	12.5
		$K = 1$	220.63384	9.124	75.94	12.5
		$K = 2$	220.62114	8.931	97.26	12.5
		$K = 3$	220.59999	8.610	132.78	25
		$K = 4$	220.57038	8.160	182.50	12.5
		$K = 5$	220.53233	7.582	246.41	12.5
HNCO	10(1, 9)–9 (1, 8)		220.58520	1.526	101.50	⋯

Notes.
[a] Einstein *A* coefficients from SPLATALOGUE (http://www.splatalogue.net/).
[b] Upper level energy, constants are from SPLATALOGUE (http://www.splatalogue.net/).
[c] Degeneracy, constants are from Wang et al. (2010).

K transitions can be used to derive the rotation—hence gas kinetic —temperature, as well as the column density. This is conventionally achieved by using the integrated line intensities of multiple transitions at different excitation levels via the rotation diagram analysis (Goldsmith & Langer 1999, and references therein). This approach, however, assumes that the line-emitting region is in LTE and is optically thin ($\tau \ll 1$). The derived quantities will be substantially affected if these conditions are not met. After a few trials of the rotation diagram analysis, we found non-negligible optical depths in the observed CH$_3$CN lines in many of our targets, leading us to choose to derive the molecular column densities and rotation temperatures through the following line profile fitting

approach. Our first assumption is that all the CH_3CN transitions considered in the fit satisfy the LTE condition and have the same LSR velocity and the same line width as derived in the previous step. We further assume the line opacity $\tau_i(\nu)$ for each transition i to be in Gaussian form, which corresponds to pure Doppler broadening:

$$\tau_i(\nu) = \tau_{i,0} \sqrt{\frac{4\ln 2}{\pi}} \exp\left(-4\ln 2 \left(\frac{\nu - (\nu_0 - \nu_{\text{off}})}{\Delta\nu}\right)^2\right). \quad (1)$$

Here, ν_0 is the rest frequency of the molecular transition, ν_{off} is the offset in frequency, and $\Delta\nu$ is the FWHM of the line profile in hertz. This equation may also be expressed in the velocity domain as follows:

$$\tau_i(v) = \tau_{i,0} \sqrt{\frac{4\ln 2}{\pi}} \exp\left(-4\ln 2 \left(\frac{v - v_{\text{LSR}}}{\Delta V}\right)^2\right). \quad (2)$$

The overall observed spectrum in brightness temperature $T_{\text{obs}}(v)$ can be expressed as

$$T_{\text{obs}}(v) = f T_{\text{rot}} \left(1 - \exp\left(-\sum_i \tau_i(v)\right)\right), \quad (3)$$

where v is the velocity against which the spectrum is measured, and v_{LSR} and ΔV are the LSR velocity and FWHM of the line derived in the first step, respectively. T_{rot} is the rotation temperature, or equivalently the molecular kinetic temperature under LTE. We also employed a filling factor f in the expression to account for the fact that the emission region may not fill the entire observing beam. The opacity of the line center $\tau_{i,0}$ for transition i is expressed as (Wang et al. 2010)

$$\tau_{i,0} = \frac{c^3}{8\pi\nu_i^3} \frac{A_{\text{ul}}}{\Delta V} \frac{g_u N_{\text{tot}}}{Q_{\text{rot}}} e^{-E_u/kT_{\text{rot}}} (e^{h\nu_i/kT_{\text{rot}}} - 1), \quad (4)$$

where c is the speed of light, ν_i is the rest frequency of transition i, A_{ul} is the Einstein A coefficient of transition i, g_u is the upper-level statistical weight of transition i, E_u is the upper-state energy level, Q_{rot} is the dimensionless rotational partition function, k is the Boltzmann constant, and h is the Planck constant. With all the other parameters being known constants, the free parameters left in the line fit are the total column density N_{tot} of CH_3CN, the rotation temperature T_{rot}, and the filling factor f.

We accommodated $CH_3^{13}CN$ $J = 12$–11 $K = 0$–5 line profiles in the fitting procedure for spectra in which the $CH_3^{13}CN$ $K = 0$ line is detected. In these cases, we assumed the same filling factor, rotation temperature, line width, and LSR velocity as their CH_3CN counterparts, and only allowed an additional free parameter, the total column density of $CH_3^{13}CN$, to vary. Finally, since the HCNO line does not seem to contaminate the nearby CH_3CN and $CH_3^{13}CN$ transitions in most cases, we appended individual Gaussians to the profile calculation for those sources with HNCO 10(1, 9)–9(1, 8) detection. The fits were done by performing χ^2 minimization between the observed and the model spectra with flat priors of $10^{-4} \leqslant f \leqslant 1$, N_{tot} of CH_3CN and $CH_3^{13}CN$ in the range from 10^{10} to 10^{19} cm^{-2}, and T_{rot} between 10 and 500 K.

4. Results

We present the spectra of the sources with CH_3CN detection in our sample in Figure 1. Those with marginal and without CH_3CN detection are shown in Figures 2 and 3, respectively.

Table 4 shows the rms noise in the observed spectra and the peak intensities of the detected CH_3CN, $CH_3^{13}CN$, and HNCO transitions. The overall detection rate of CH_3CN $J = 12$–11 in our sample is 43% (24 out of 56), while the detection rate in EGOs is 54% (19 out of 35). Six sources are marginally detected with CH_3CN, and the remaining 26 sources have no CH_3CN detection ($\lesssim 2.5\sigma$).

In Table 5 we list the best-fit parameters, including the spectral line FWHM, filling factor, CH_3CN column density, and rotation temperature derived from line profile fitting. The opacity of the line center of CH_3CN $J = 12$–11 $K = 0$ is also shown in Table 5. We measured a mean FWHM of 6.5 km s^{-1} with a standard deviation of 2.0 km s^{-1} in our sample. The derived gas temperatures for the sources with CH_3CN detection range from 40 to 300 K with the exception of G49.42–AK, which has a derived temperature of $T \sim 10$ K. The column densities range from 10^{12} to 10^{17} cm^{-2}. Assuming the detected CH_3CN emitting regions are spherical with uniform density, we estimate the total molecular mass and average gas volume density based on the kinematic distances estimated by He et al. (2012), the filling factors, and column densities obtained from our fitting, assuming a CH_3CN/H_2 abundance ratio of 10^{-9}. These results are also shown in Table 5. In addition, among the 24 sources with CH_3CN detection, we found that nine sources have discernible ^{13}C-bearing isotopologue $CH_3^{13}CN$ $J = 12$–11 emission, and 10 sources with HNCO 10(1, 9)–9(1, 8) detection. We also report these derived $CH_3^{13}CN$ column densities in Table 5.

5. Discussion

5.1. Detection Statistics

High detection rates were found previously in several surveys of CH_3CN toward MSFRs selected with different criteria. For example, Araya et al. (2005) surveyed a sample of 17 sites of massive star formation that were selected based on detection of the tracer of high density, CS. They found CH_3CN detection in at least one of the J-level transitions among $J = 5$–4, 6–5, 8–7, and 12–11 toward all the sources in their sample. Purcell et al. (2006) also reported a 70% detection rate of CH_3CN emission in a methanol maser-selected sample of MSFRs.

As in this work, Pankonin et al. (2001) conducted a CH_3CN $J = 12$–11 survey with the SMT (known at the time as the Heinrich Hertz Telescope of the SMT Observatory). Their target sample was considered as a representative group of known or suspected regions of massive star formation with characteristics including known radio continuum emission from ultracompact H II regions, compact submillimeter or FIR continuum emission from dust, known massive CO outflows, or methanol maser emission. Among the 48 targets in their sample, 25 were detected with the CH_3CN $J = 12$–11 lines with a mean FWHM of 7.7 km s^{-1} and a standard deviation of 3.0 km s^{-1}.

The most recent study of CH_3CN $J = 12$–11 in massive protostellar candidates was done by Rosero et al. (2013), also with the SMT. Their sample consists primarily of prominent HMC sources with large *IRAS* luminosities. Out of 21 targets, their observations resulted in nine detections of the CH_3CN $J = 12$–11 lines with FWHM line widths ranging from 5 to 8 km s^{-1}. In fact, four of the sources in our survey overlap with the sample of Rosero et al. (2013). The duplicate targets are G16.59–0.05, IRAS 18264–1152 (G19.88–0.53 in our list), G23.01–0.41, and G34.26+0.15. For the former three
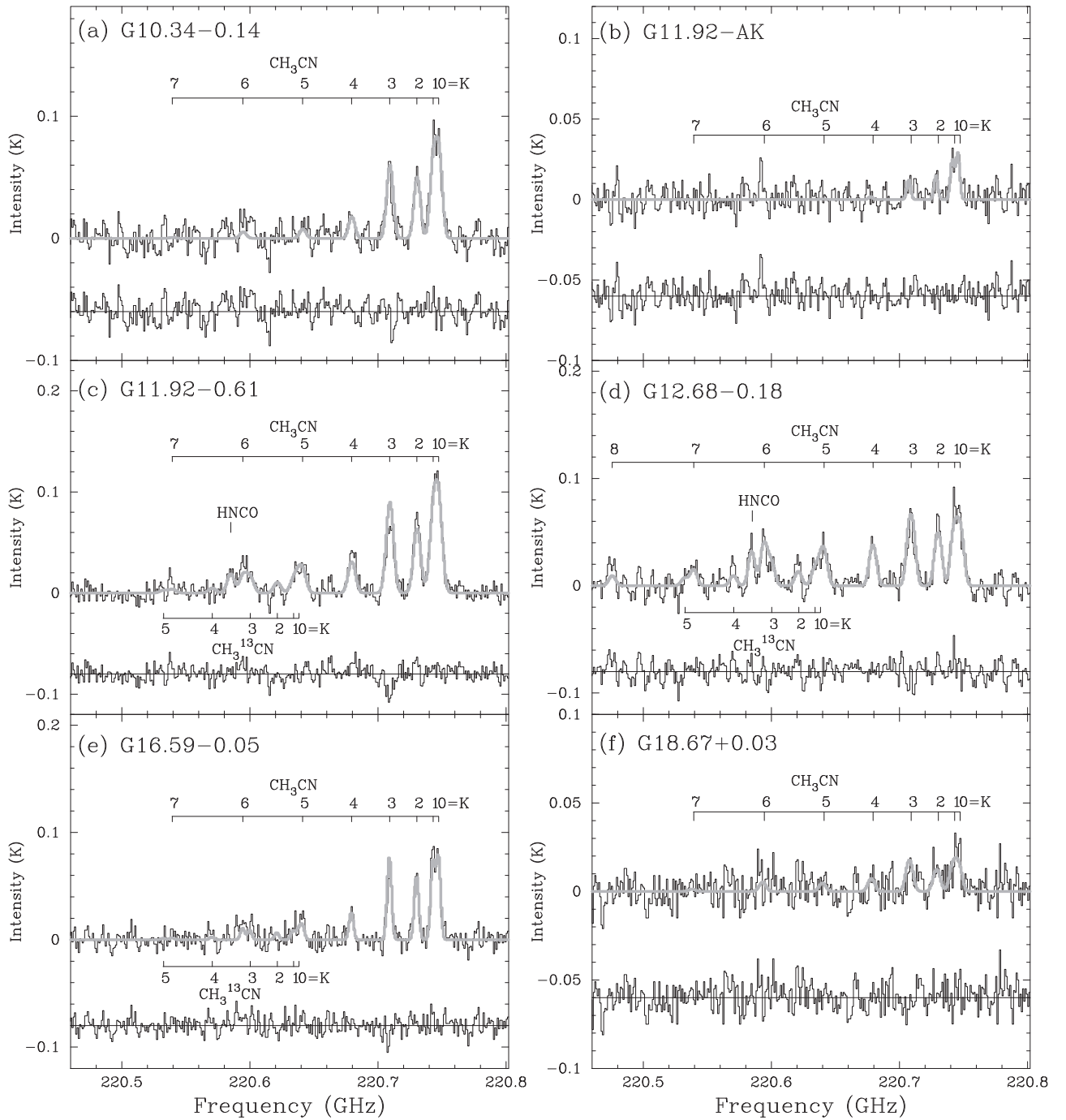
Figure 1. Spectra of sources with CH_3CN detection. For each panel, the upper part shows the observed spectrum (black) and the best fitted synthetic spectrum (gray) while the bottom part presents the fitting residual. Locations of the CH_3CN $J = 12-11$ $K = 0-8$ transitions, as well as the $CH_3^{13}CN$ and HNCO transitions, if applicable, are marked.

objects, the observed positions differ between the two surveys by less than $5''$ and the observed spectra are fully consistent. In the case of G34.26+0.15, Rosero et al. (2013) centered toward the HMC nominal position at $(18^h53^m18\overset{s}{.}5, 01°14'58)$ while we pointed toward the EGO position reported by Cyganowski et al. (2008) at $(18^h53^m16\overset{s}{.}4, 01°15'07)$, which is about half an arcminute northwest from the HMC. Therefore, our observed peak intensity of G34.26+0.15 is only 10% of that observed by Rosero et al. (2013). Despite the difference in sample selection and limited statistics, our detection rate of CH_3CN appears to be comparable to that in the aforementioned studies.

Pankonin et al. (2001) suggested that the non-detection of CH_3CN in the sample does not necessarily reflect the absence of hot CH_3CN gas. For example, a large beam dilution factor may cause the emission to fall below the sensitivity. A similar reason could explain some, if not all, of the non-detections of CH_3CN in our sample. In fact, six sources in our sample have the sum of $K = 0$ and $K = 1$ line intensities exceeding 2.5σ but below 3σ. We consider these sources as marginal rather than completely lacking CH_3CN. While stacking these six spectra weighted by inverse variance, we found significant CH_3CN detection up to $K = 7$ transition in the stacked
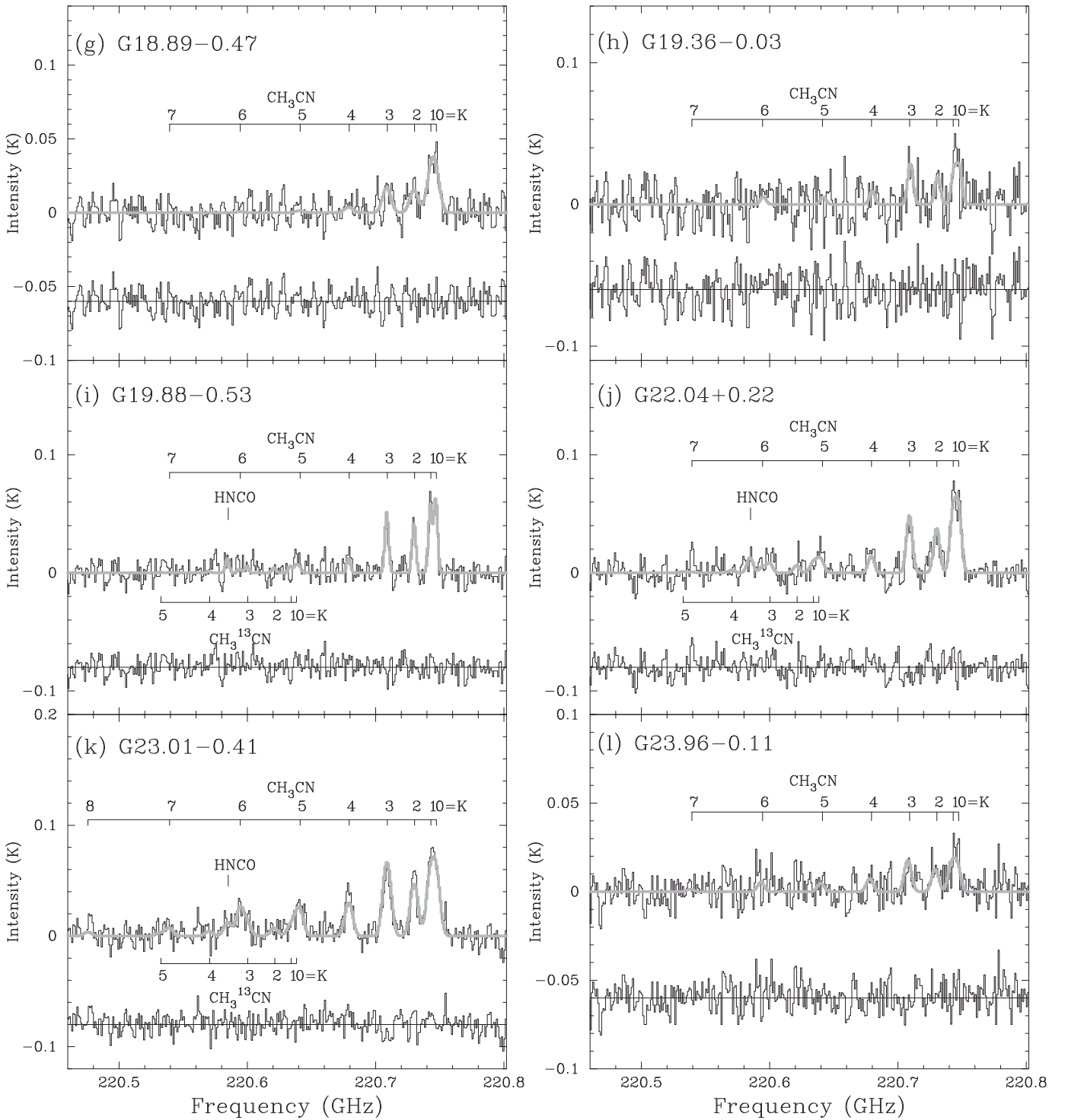
Figure 1. (Continued.)

spectrum. This finding supports our speculation that these sources do have weak CH_3CN $J = 12$–11 emission that may be diluted below the sensitivity limit by the large beam size. This may also explain why G19.01, which is only marginally detected with CH_3CN in our survey, is readily detected in the same J-level in interferometric observations with high angular resolution (Cyganowski et al. 2011b). We also stacked the spectra of the 26 sources without CH_3CN detection in the same manner. The stacked spectrum shows faint CH_3CN emission up to only the $K = 3$ transition. Higher K transitions are probably

buried in the large noise even after the stacking approach has reduced the noise level to $\sigma/\sqrt{26}$.

We did not find any correlation between the observed CH_3CN line intensities and the source distances or the physical quantities such as total gas mass. Furthermore, there is no correlation in the line luminosities between CH_3CN and $H^{13}CO^+$ (3–2), which is a tracer of dense gas with a critical density $\sim 2.11 \times 10^6$ cm^{-3} similar to that of CH_3CN (He et al. 2012). In short, the fraction (54%) of EGOs readily detected with CH_3CN transitions is likely a lower limit given the
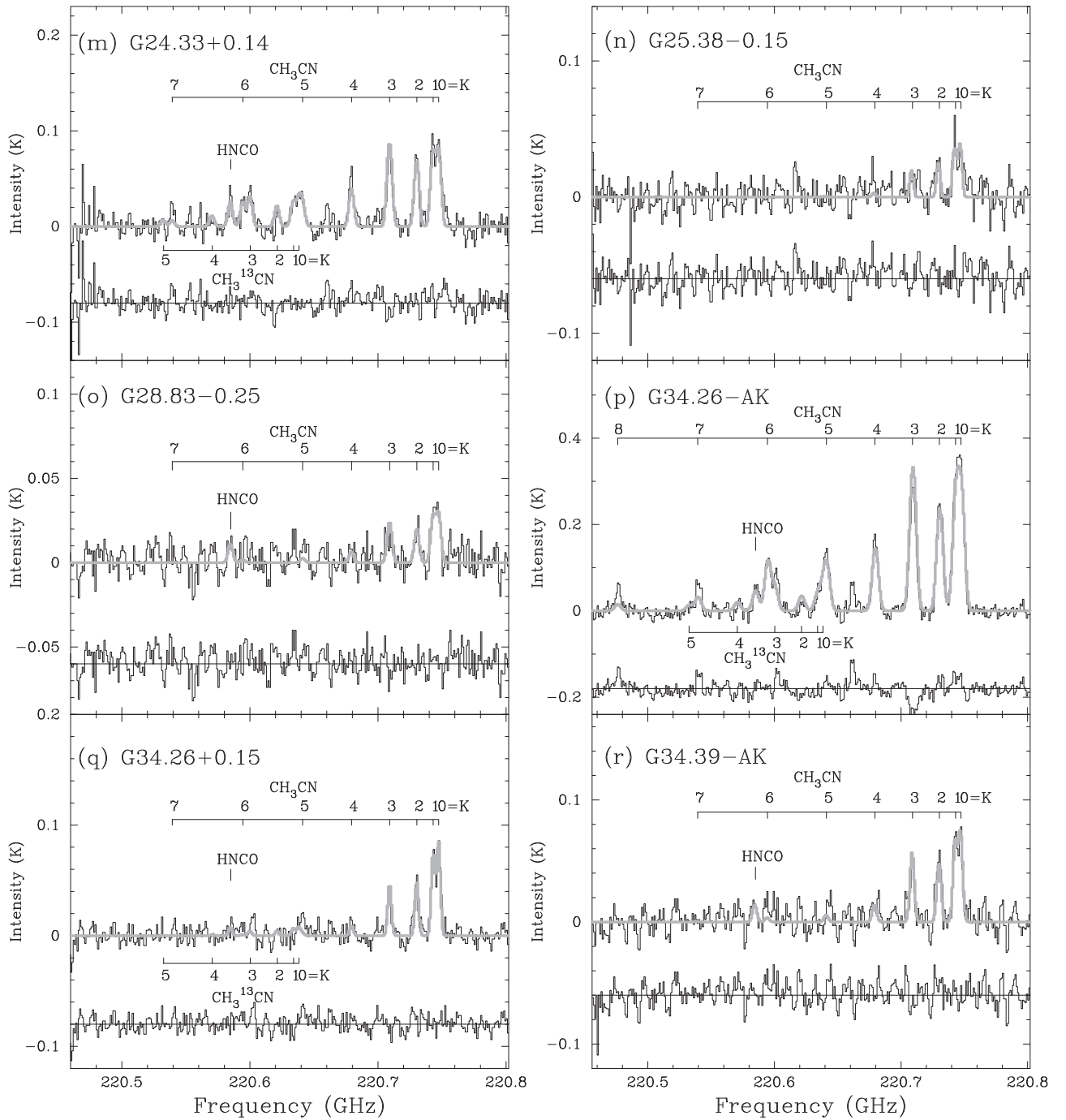
Figure 1. (Continued.)

sensitivity limit of SMT. However, the non-detection of CH_3CN $J = 12–11$ could still be due to the nature of the source. The non-detections are most easily explained if warm CH_3CN is entirely absent from the source.

In previous studies, five sources, G16.59–0.05, G19.61–0.23, G23.01–0.41, G34.26+0.15, and G35.03–0.35, have been found to harbor HMCs (De Buizer et al. 2003; Sanna et al. 2010a, 2010b; Brogan et al. 2011), as expected from the presence of CH_3CN emission lines. Interferometric observations have resolved multiple millimeter/centimeter sources in G11.92–0.61, G28.83–0.25, G35.03+0.35, and G45.47+0.05 (Wilner et al. 1996; Cyganowski et al. 2011a, 2011b).

For sources with *AKARI* counterparts, there is neither an obvious higher detection rate nor stronger CH_3CN emission toward the *AKARI* sources. We consider this as a lack of evidence for associating *AKARI* bright sources as the outflow-driving source of the EGOs.

5.2. Usage and Limitation of the Line Profile Fitting Analysis

We use G23.01–0.41 as an example to illustrate the differences between our profile fitting approach and the rotation diagram analysis. The left panel in Figure 4 shows the rotation diagram of G23.01–0.41. The right panel shows the spectrum generated by adopting the column density and
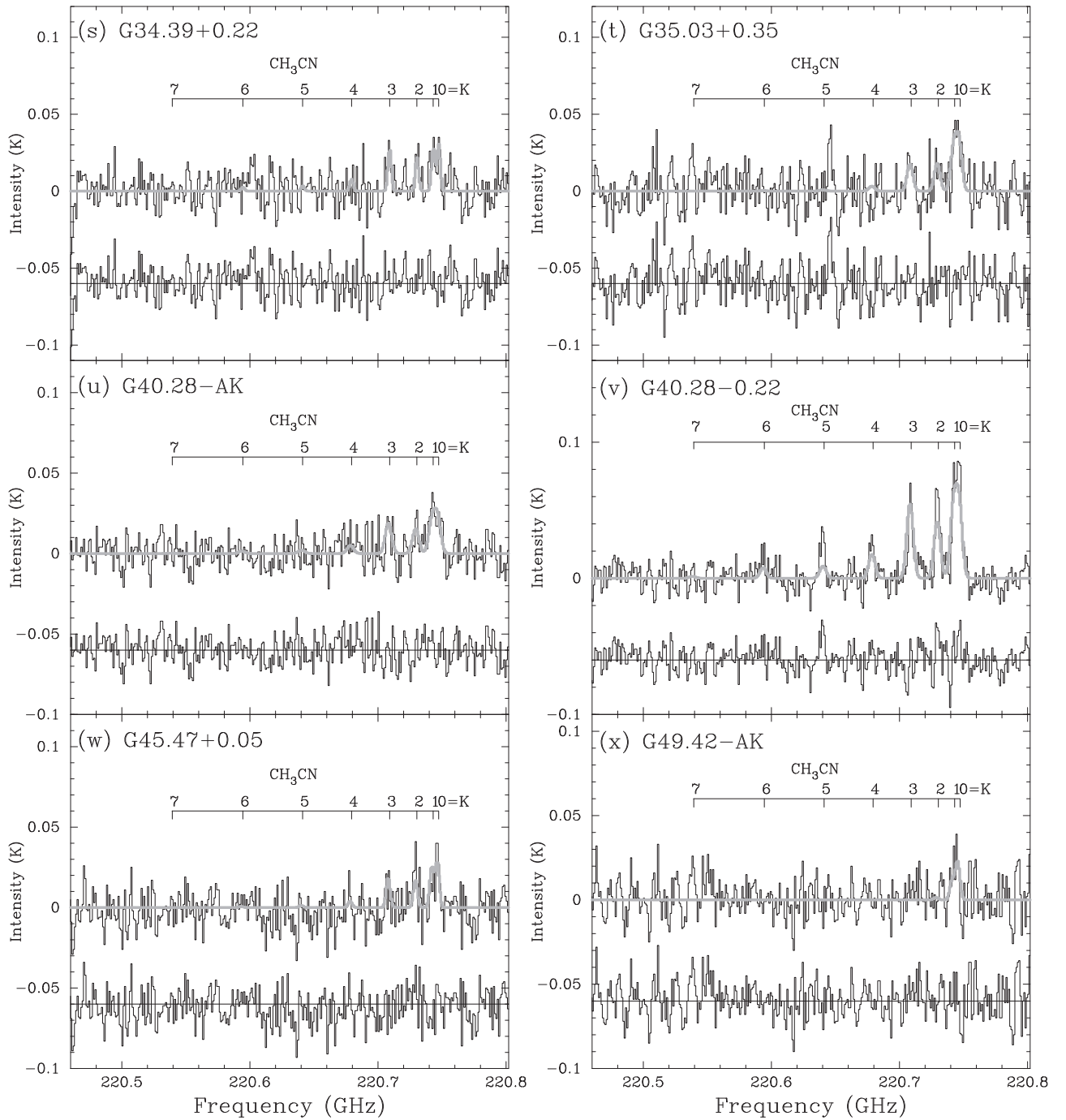
Figure 1. (Continued.)

temperature derived from the rotation diagram (red dotted line) and those generated with parameters derived from our profile fitting method (gray solid line). It is noticed that the peak intensity of the $K = 3$ transition is significantly overestimated by the red dotted line from the rotation diagram analysis. Meanwhile, the observed data points for the $K = 3$ and $K = 6$ transitions lie well below the best-fit line in the rotation diagram, which is systematically seen in several other sources in our sample.

Without the beam dilution effect, the CH_3CN column density estimated through the rotation diagram analysis is $1.3^{+0.3}_{-0.2} \times 10^{13}$ cm^{-2}. The derived temperature 292^{+496}_{-65} K has asymmetric errors and is higher than the temperature

(193 ± 21 K) derived from our line profile fitting method. All the evidence indicates appreciable optical depth in the lower K transitions as discussed by Goldsmith & Langer (1999). Indeed, the line-center optical depths of the $K = 3$ and $K = 6$ transitions in G23.01–0.41 are 1.2–3.7 times larger than those of their adjacent transitions when evaluated using the parameters derived from the profile fitting method. The population diagram analysis developed by Goldsmith & Langer (1999) incorporates an optical depth correction factor of $\ln C_\tau$ in the original rotation diagram, where
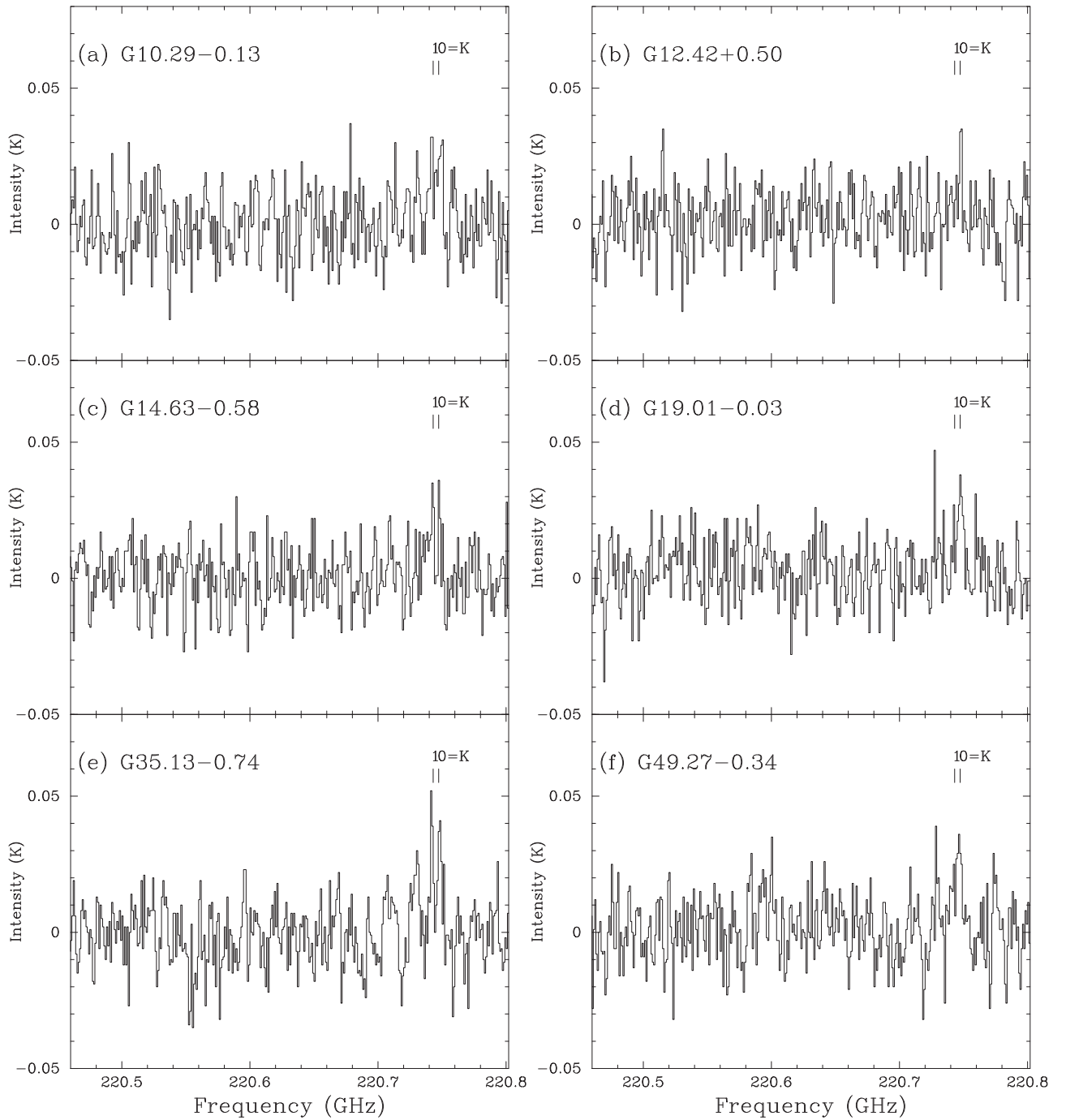
$$C_\tau = \frac{\tau}{1 - e^{-\tau}}. \tag{5}$$

Figure 2. Spectra of sources with marginal CH_3CN detection. For each panel, the observed spectrum and the expected location of the CH_3CN $J = 12$–11 $K = 0$ and $K = 1$ transitions are shown.

When the optically thick lower K transitions are corrected with the $\ln C_\tau$ term in the rotation diagram, the linear fit becomes steeper and the derived temperature is reduced to a temperature that is consistent with that derived from our line profile fitting method.

While the optical depths estimated from our line profile model are not negligible, they remain of the order of a few. We speculate that while our approach is able to recover some optical depth effects, it is possible that our method still underestimates the optical depth. In our profile fitting method, as the optical depth increases, the originally Gaussian synthetic line profile formulated in Equation (2) becomes boxy, or flat-topped in shape. This flat-topped line profile is not present in any of the spectra we

observed. Our fitting method therefore might have prevented optical depths from increasing substantially since the mismatched line shapes could lead to larger χ^2 values.

5.3. Gas Temperatures, Source Sizes, and CH_3CN Column Densities

The molecular gas temperature is responsible for the line intensity ratios between different K components and can be derived from spectral line fitting. Since the energy level of the CH_3CN $J = 12$–11 $K = 0$ line is 68.9 K, it is expected that thermal emission of the $J = 12$–11 transitions best probes regions of warm temperature. As mentioned in Section 4, for
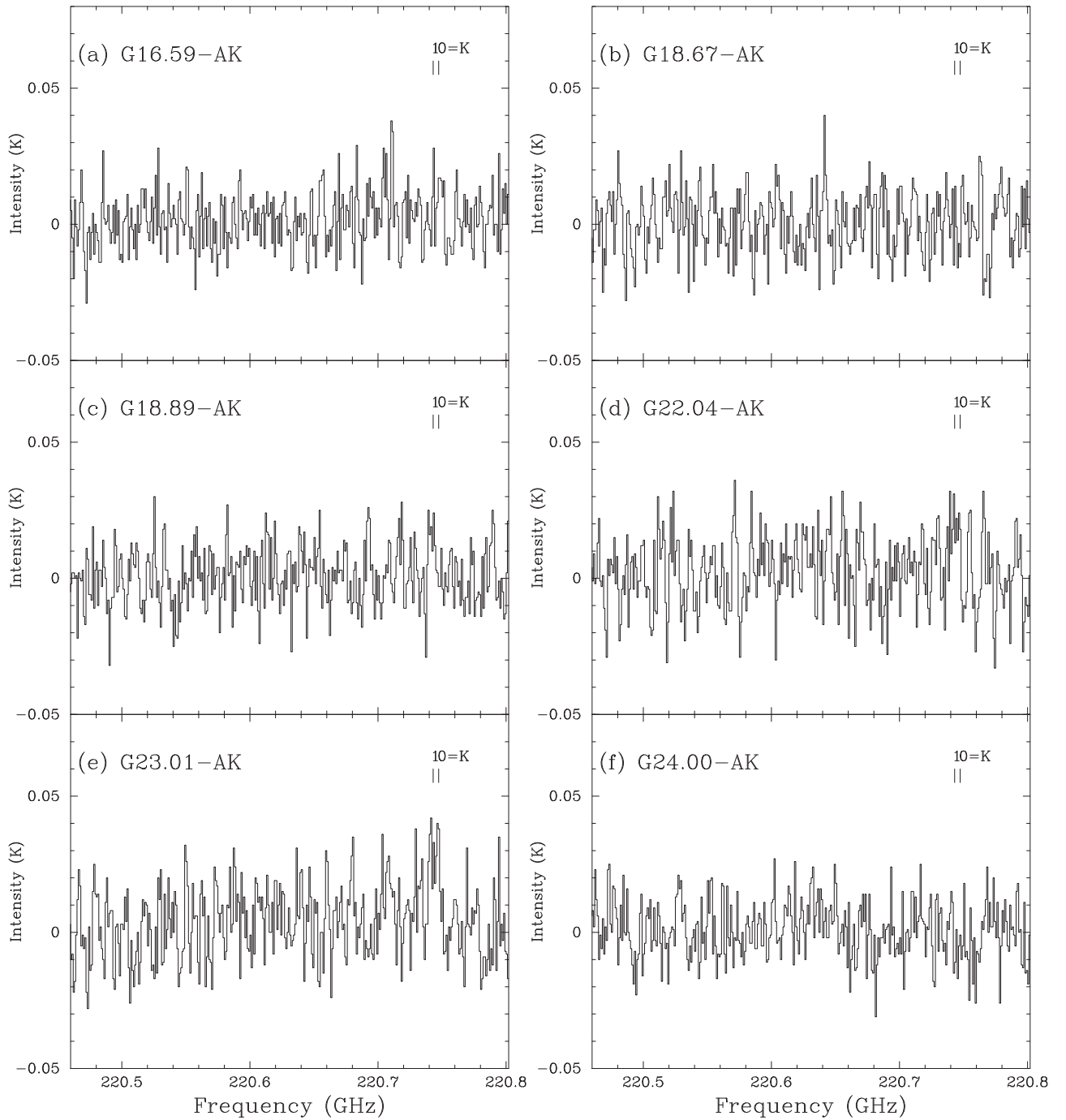
Figure 3. Spectra of sources with no CH_3CN detection. For each panel, the observed spectrum and the expected locations of the CH_3CN $J = 12$–11 $K = 0$ and $K = 11$ transitions are shown.

the sources with CH_3CN detection, we derived gas temperatures spanning mostly from 40 to 300 K. The temperature range implies CH_3CN residing in a warm to hot environment. The only exception occurs in G49.42–AK, which has an estimated gas temperature of only 10 K. The relatively low signal-to-noise ratio (S/N) of the detection is possibly causing this low temperature and a very large fractional error.

The filling factors and the column densities obtained from the spectral fitting range mostly from 10^{-4} to 10^{-2} and from 10^{12} cm^{-2} to 10^{17} cm^{-2}, respectively. One may notice from Table 4 that most sources have CH_3CN column densities ranging from 10^{14} to 10^{17} cm^{-2}. The exceptions are the five

sources (G18.89–0.47, G19.36–0.03, G34.26+0.15, G35.03 +0.35, and G49.42–AK) with a unity filling factor and column densities of the order of a few $\times$ 10^{12} cm^{-2}. In the regime of low column density, the CH_3CN emission becomes optically thin in these sources. As pointed out by Su et al. (2009), filling factor and column density become degenerate in the optically thin limit and therefore cannot be determined individually.

The small filling factors spanning from 10^{-4} to 10^{-2} for nearly all sources suggest that CH_3CN emitting regions are rather compact as compared to the 34″ beam size of the telescope. Given the source distances, the inferred linear sizes of emission regions range from 0.02–0.08 pc (4000–16,000 au), which is comparable
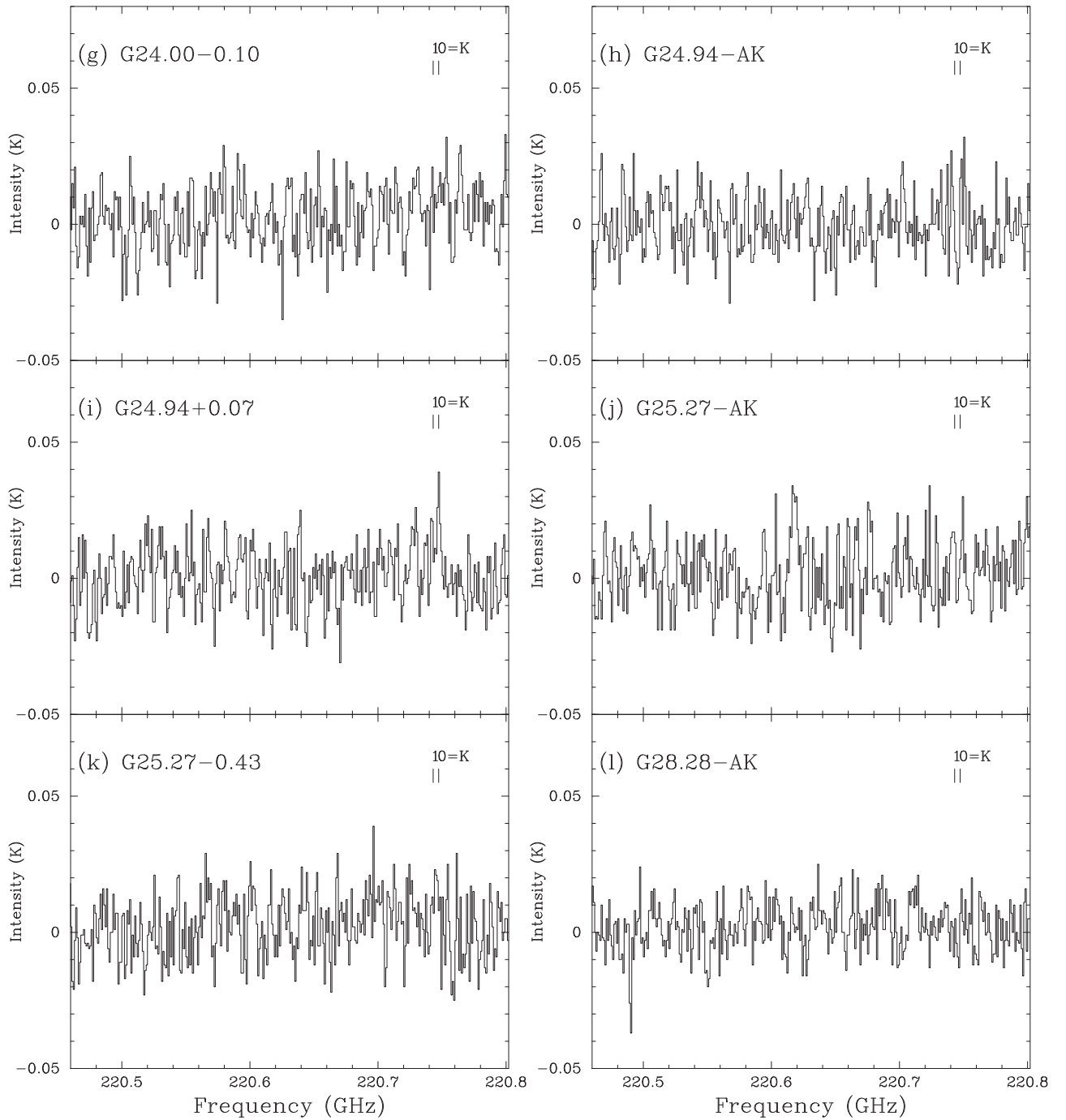
Figure 3. (Continued.)

to those of typical hot cores ($\sim$0.1 pc) and hyper-compact H II regions ($\leqslant$0.05 pc). Indeed, higher-resolution observations with the Submillimeter Array (SMA) toward a few of our targets have shown that the CH_3CN emission appears to be very compact (Cyganowski et al. 2011b; Hernández-Hernández et al. 2014; Ilee et al. 2016). In Cyganowski et al. (2011b), the size of the CH_3CN emitting region of G11.92–0.61 is estimated to be 0.02 pc. A gas temperature of 166 K in G11.92 was also estimated from the rotation diagram analysis of the CH_3OH transitions after iteratively solving the optical depth correction factor (Cyganowski et al. 2011b). With a two-component fit, the authors estimated the CH_3CN emitting regions to be 0.06 pc and 0.01 pc for the cold ($\sim$77 K) and warm ($\sim$166 K) components, respectively. These

source sizes and gas temperatures are very similar to our derived source size ($\sim$0.06 pc) and gas temperature (130 K) for this object. From follow-up higher-resolution imaging toward G11.92–0.61 MM1, Ilee et al. (2016) further deduced two components with higher temperatures of 150 and 230 K from CH_3CN emission, which likely traces a rotating disk of a few thousand astronomical units in size. The latter implies a smaller filling factor/size than what we have derived. In another example, Cyganowski et al. (2012) reported a gas temperature of 175 K derived from CH_3CN transitions in G18.67+0.03 that is also consistent with the temperature we derived (162 K). We do not compare our derived size with them since the low S/N in higher K transitions in our spectrum gives rise to an ill-constrained filling factor.
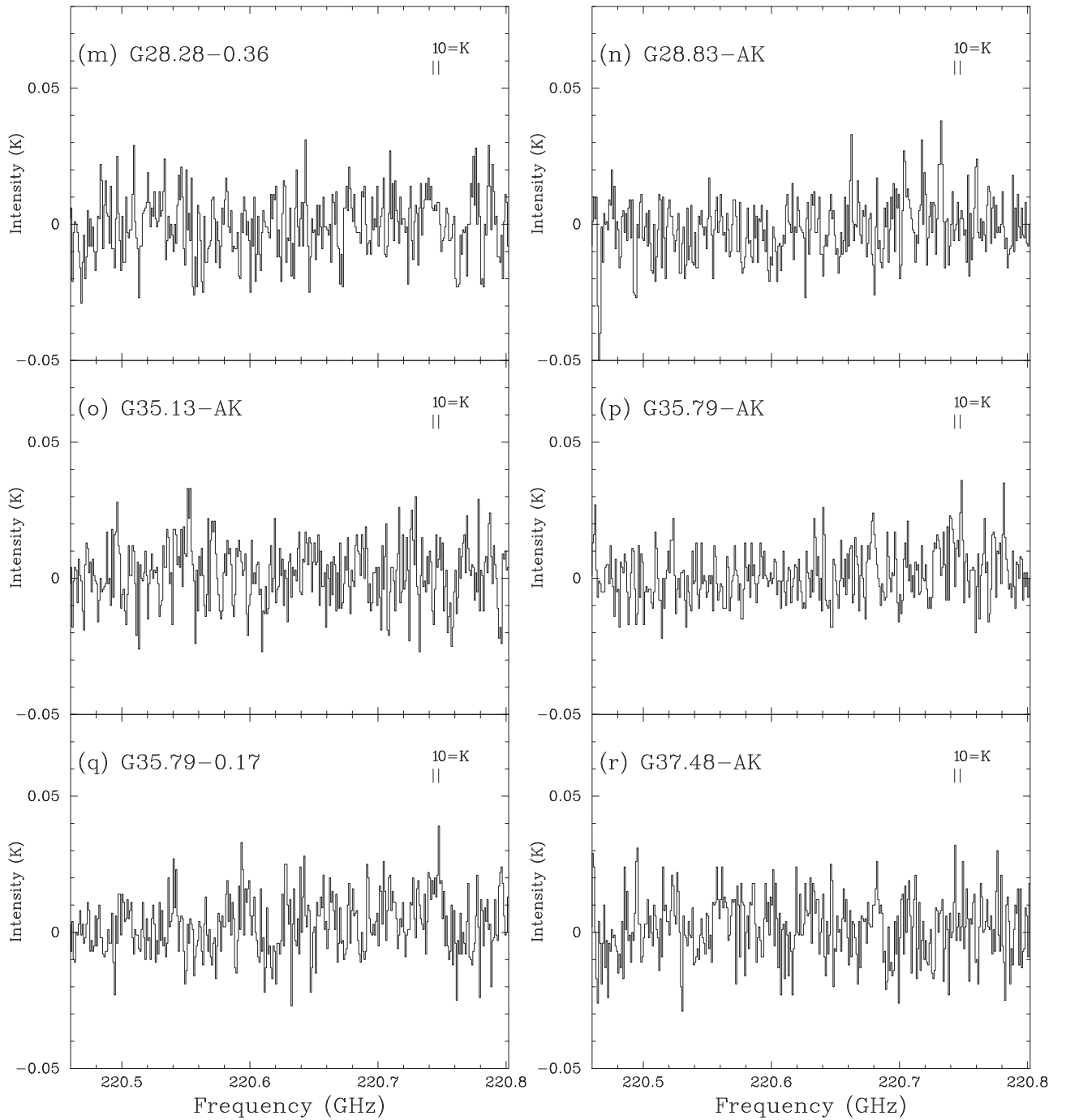
Figure 3. (Continued.)

Similar comparisons can also be made between our work and the archival study of SMA observations of the CH_3CN $J = 12$–11 lines toward 17 HMCs conducted by Hernández-Hernández et al. (2014). Three of their sources overlap with our sample—IRAS 18182–1433 (or I18182 in their paper and G16.59–0.05 in our list), G23.01–0.41, and G45.47+0.05. Similarly to Cyganowski et al. (2012), Hernández-Hernández et al. (2014) adopted a two-component (hot and cold) scheme in their line profile fitting. They reported source sizes of $1\rlap{.}''1$ ($\sim$0.002 pc) and $4\rlap{.}''4$ ($\sim$0.008 pc) and temperatures of 219 K and 75 K for the hot and cold components in I18182, respectively. Our derived temperature of 102 K for G16.59–0.05 falls within their temperature range. On the other

hand, our derived source size (0.04 pc) overestimates the actual CH_3CN emitting region by a factor of 5.

For G23.01–0.42, Hernández-Hernández et al. (2014) derived temperatures of 237 and 58 K for the hot and cold components respectively. The emission sizes are estimated to be $1\rlap{.}''2$ ($\sim$0.004 pc) and $4\rlap{.}''0$ ($\sim$0.015 pc) for the two components. Similarly, our derived gas temperature of 193 K for this source is bracketed by their two-component temperatures and our source size of 0.02 pc is larger than the sizes inferred from their observations.

In G45.47+0.05, Hernández-Hernández et al. (2014) found gas temperatures of 155 and 65 K for the hot and cold components. For this object, our estimated gas temperature of
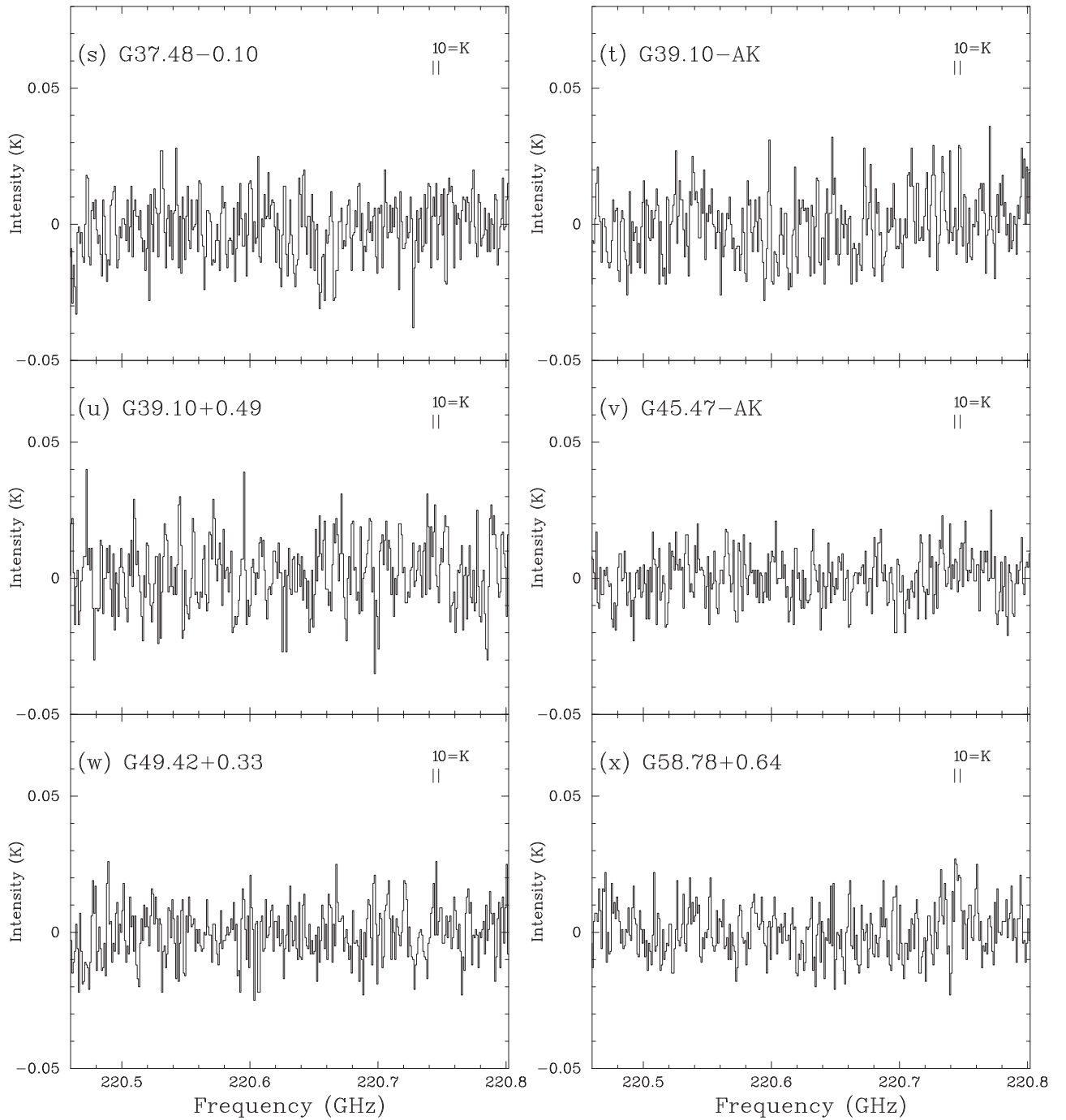
13

Figure 3. (Continued.)

62 K is more consistent with their cold component. Given that the CH$_3$CN lines appear to be optically thin, we inferred a filling factor of unity and are thus unable to constrain the source size in G45.47+0.05. Given the different approaches in the analysis and the associated uncertainties, we consider the temperatures extracted from the two studies to be comparable, though the sources are found to be more compact from the SMA study. In fact, the even smaller filling factors and compact CH$_3$CN emitting regions inferred from interferometric observations are not unusual. Observations with the SMA toward the ultracompact H II region G5.89–0.39 by Su et al. (2009) found small filling factors between 0.02 and 0.24 in the same set of CH$_3$CN lines with an interferometric beam size of

$3\rlap.''1 \times 1\rlap.''8$. The results imply that CH$_3$CN traces a highly clumpy medium at smaller physical scales.

5.4. CH$_3$CN Line Widths

In Table 6, the derived line widths of the detected CH$_3$CN emission range from 4 to 10 km s^{-1}, with a mean of 6.5 km s^{-1}. We list and compare these observed line widths with those of HCO$^+$, H^{13}CO$^+$, CO, ^{13}CO, C^{18}O, and CH$_3$OH previously observed (Chen et al. 2010; He et al. 2012). As shown in Figure 5, no clear correlation is noticed in these plots. This is expected since different molecular species trace different physical components and may be affected by their
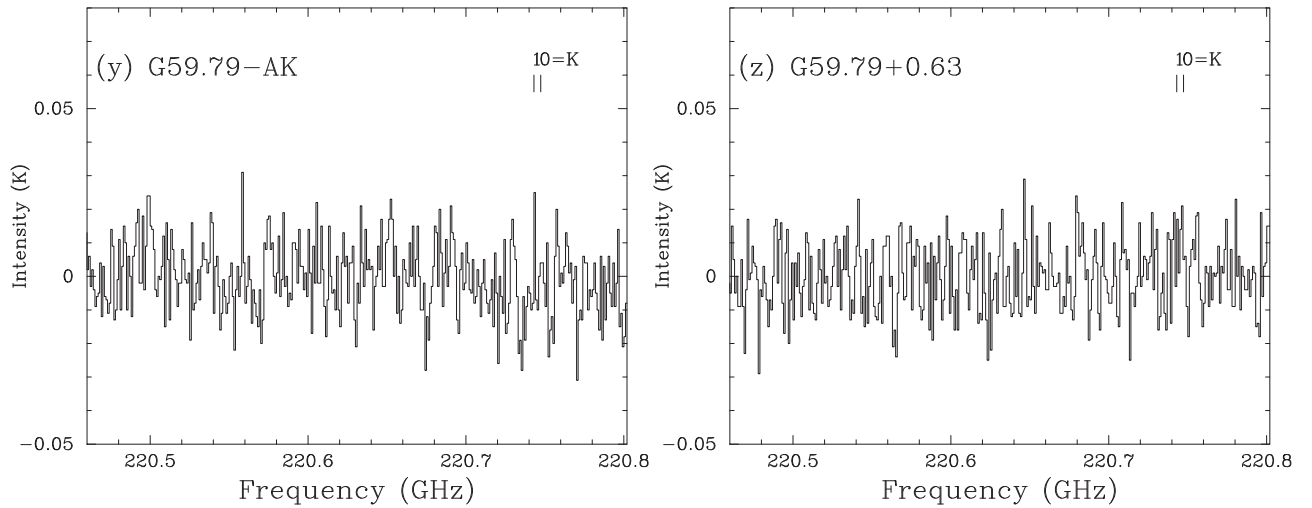
Figure 3. (Continued.)

opacities at different levels. For example, CH_3CN could be trace very compact torus/rotating disks, as have been observed in several massive star-forming cores (Beltrán et al. 2005, 2011), while CO and its isotopologues as well as other tracers of dense gas (such as HCO^+ and $H^{13}CO^+$) are likely outlining the large-scale dense envelopes/clumps, if not affected by molecular outflows. Emission from CO and its isotopologues tends to be optically thick, particularly toward MSFRs. The significance of these effects would vary from target to target. Furthermore, although both are warm gas tracers, CH_3CN may not form in the same region as CH_3OH. This is believed to be a result of chemical evolution, where CH_3CN forms at a later stage than CH_3OH. Recent observations of G33.92+0.11 by Minh et al. (2016) have revealed a range of CH_3OH/CH_3CN abundance ratios in different cores with ALMA, which supports this scenario. Considering all these possibilities, there may not be correlations between CH_3CN and these molecular emissions in their line widths.

On the other hand, the CH_3CN line widths appear to be broader than those of HCO^+, ^{13}CO, $H^{13}CO^+$, and $C^{18}O$. The breadth of the CH_3CN lines in turn contributes to the larger virial masses, which we discuss in detail in Section 5.5.

5.5. Gas Masses, Densities, and the Origin of CH₃CN Emission

By assuming a CH_3CN fractional abundance of 10^{-9} (Su et al. 2009), we derived total molecular masses from a few $M_\odot$ to a couple hundred $M_\odot$ traced by CH_3CN in the sample. We estimated the average molecular gas densities to range from 10^6–10^9 cm^{-3} provided the source sizes are on sub-parsec scale. For those five sources with unity filling factor, the average molecular gas density is $\sim 10^3$ cm^{-3} but will reach the level of $\sim 10^7$ cm^{-3} if sub-parsec source sizes are adopted. Given that the critical density of the CH_3CN $J = 12$–11 transitions is approximately 10^6 cm^{-3} or larger, such high gas densities are supportive of CH_3CN being predominantly thermally excited and are fully consistent with the line profile fitting assumptions. Virial masses of the CH_3CN emitting gas can also be estimated from the derived line widths and source sizes. Assuming spherical geometry, the virial masses of these sample targets span from several hundred to thousands of solar masses, and the corresponding gas densities would be 10^8 and 10^{10} cm^{-3}. Note that here we do not discuss the six optically thin cases since their sizes cannot be determined. In Table 5,

we use the upper limits of their sizes for calculation, which results in extraordinarily large virial masses.

Previous observations of CH_3CN suggested its emission being mostly associated with HMCs in star-forming regions (e.g., Araya et al. 2005). CH_3CN is likely liberated in the gas phase due to heating of the icy mantles on dust grains by embedded YSOs (Millar et al. 1997). Interferometric observations with higher angular resolution toward massive YSOs also found that CH_3CN has elongated morphology with a velocity gradient often perpendicular to the bipolar molecular outflows associated with these YSOs. Such signatures are considered to show CH_3CN residing in rotational disks or tori around the central YSOs (e.g., Beltrán & de Wit 2016, and references therein). On the other hand, CH_3CN has also been found in the dense molecular envelope/cocoon around ultracompact H II regions (Su et al. 2009) and has been suggested as a tracer of outflow/shock activities as well (Codella et al. 2009).

Based on our estimates, the observed CH_3CN gas is unbound and traces very energetic components, likely outflow or shocks in our targets. Previously, Codella et al. (2009) studied the outflows associated with the low-mass protostar L1157–mm, where CH_3CN was detected in the blueshifted lobe. They considered CH_3CN being produced by the passage of bow shocks. In MSFRs, Leurini et al. (2011) reported similar values in line widths (~ 8 km s^{-1}) and velocity gradients in HNCO and CH_3CN in IRAS 17233–3606. The similarity in kinematics suggests that the two species may be tracing the same volume of gas. Further study by Rodríguez-Fernández et al. (2010) reported strong detection of HNCO in the shock environment in the L1157 molecular outflow, which also exhibits the same characteristics as other well-known shock tracers. Given the possibility that HNCO is a tracer of interstellar shocks, CH_3CN may also be associated with shocks and outflows in L1157. A recent interferometric study toward the massive O-type star G17.64+0.19 also revealed CH_3CN tracing plume-/arc-like structures, possibly the cavity working surfaces due to wide-angle interactions of wind with the dense molecular envelope (Maud et al. 2018).

It is noteworthy that in our observations, a correlation between $CH_3^{13}CN$ and HNCO line intensities can be discerned (Figure 6). This would be expected if HNCO and CH_3CN reside in similar environments and the observed HNCO and $CH_3^{13}CN$ are optically thin. Furthermore, as shown in Figure 5, the majority of our CH_3CN line widths are larger than

Table 4
Observational Noise Level and Peak Intensities

Object	rms[a] (mK)	CH_3CN Peak[b] (mK)	$CH_3^{13}CN$ Peak[b] (mK)	HNCO Peak (mK)
G10.29–0.13	11.7	⋯	⋯	⋯
G10.34–0.14	8.4	97	⋯	⋯
G11.92–AK	6.2	32	⋯	⋯
G11.92–0.61	6.9	121	30	19
G12.42+0.50	9.9	⋯	⋯	⋯
G12.68–0.18	8.9	92	50	32
G14.63–0.58	10.2	⋯	⋯	⋯
G16.59–AK	10.7	⋯	⋯	⋯
G16.59–0.05	7.3	87	27	⋯
G18.67–AK	11.0	⋯	⋯	⋯
G18.67+0.03	7.6	33	⋯	⋯
G18.89–AK	10.3	⋯	⋯	⋯
G18.89–0.47	7.7	48	⋯	⋯
G19.01–0.03	10.2	⋯	⋯	⋯
G19.36–0.03	12.2	50	⋯	⋯
G19.88–0.53	12.2	69	20	12
G22.04–AK	12.5	⋯	⋯	⋯
G22.04+0.22	7.9	78	31	13
G23.01–AK	12.1	⋯	⋯	⋯
G23.01–0.41	8.1	80	33	12
G23.96–0.11	6.7	38	⋯	⋯
G24.00–AK	10.0	⋯	⋯	⋯
G24.00–0.10	10.8	⋯	⋯	⋯
G24.33+0.14	9.7	97	37	26
G24.94–AK	9.7	⋯	⋯	⋯
G24.94+0.07	11.3	⋯	⋯	⋯
G25.27–AK	11.9	⋯	⋯	⋯
G25.27–0.43	11.1	⋯	⋯	⋯
G25.38–0.15	8.9	60	⋯	⋯
G28.28–AK	8.3	⋯	⋯	⋯
G28.28–0.36	10.8	⋯	⋯	⋯
G28.83–AK	9.9	⋯	⋯	⋯
G28.83–0.25	7.4	36	⋯	11
G34.26–AK	17.4	360	145	47
G34.26+0.15	6.6	86	17	7.6
G34.39–AK	8.8	78	⋯	14
G34.39+0.22	9.9	35	⋯	⋯
G35.03+0.35	11.9	46	⋯	⋯
G35.13–AK	10.6	⋯	⋯	⋯
G35.13–0.74	11.4	⋯	⋯	⋯
G35.79–AK	8.9	⋯	⋯	⋯
G35.79–0.17	10.0	⋯	⋯	⋯
G37.48–AK	11.3	⋯	⋯	⋯
G37.48–0.10	11.0	⋯	⋯	⋯
G39.10–AK	11.3	⋯	⋯	⋯
G39.10+0.49	12.1	⋯	⋯	⋯
G40.28–AK	8.8	38	⋯	⋯
G40.28–0.22	8.5	86	⋯	⋯
G45.47–AK	8.4	⋯	⋯	⋯
G45.47+0.05	9.9	41	⋯	⋯
G49.27–0.34	10.7	⋯	⋯	⋯
G49.42–AK	10.4	39	⋯	⋯
G49.42+0.33	9.0	⋯	⋯	⋯
G58.78+0.64	8.7	⋯	⋯	⋯
G59.79–AK	10.3	⋯	⋯	⋯
G59.79+0.63	10.2	⋯	⋯	⋯

Notes.
[a] rms noise level estimated from fitting.
[b] Peak intensities of CH_3CN and $CH_3^{13}CN$. We measure the peak intensities between the frequencies of the two lowest K components for both CH_3CN and $CH_3^{13}CN$ $J = 12$–11 since $K = 0$ and $K = 1$ components are blended.

$HCO^+(1$–0) line widths reported in Chen et al. (2010). It is thus possible that CH_3CN may be tracing the higher-velocity and energetic part of the outflow in close proximity to the YSOs.

A few possibilities, however, may lead to our derived virial masses of the CH_3CN gas greatly exceeding the gas masses estimated based on the CH_3CN emission intensities/abundances. First, we may have overestimated the virial masses (or line widths) due to the presence of (multiple) unresolved components even if the CH_3CN gas is in fact virialized and residing in the disk/torus around YSOs as previously observed. For example, Chen et al. (2006) have resolved the case of $W3(H_2O)$ as a massive protobinary system, where the two emitting sources bear CH_3CN $J = 12$–11 line widths of 2.7 and 3.6 km s^{-1} but have a separation of 2.81 km s^{-1} between them. A previous study utilizing the IRAM interferometer on the Plateau de Bure reported a linear span of 10 km s^{-1} in velocity gradient within a region of $1''$ across the hot core in $W3(H_2O)$ (Wink et al. 1994; Wyrowski et al. 1997). In this case, the single-dish data would have overestimated the virial mass if the system is unresolved. Likewise, if we assume that most of our sources have unresolved multiple components and that the line widths are only half of our derived values for each component, the virial masses will be reduced to a quarter of the original values, yielding comparable values in these two masses.

A second possibility is that the CH_3CN emitting gas resides in a compact component and an extended one as in the example of G11.92–0.61 (Cyganowski et al. 2011b; Ilee et al. 2016). The virial mass may be overestimated if our single-component line measurement is sensitive to the large and extended component in terms of the size of the emission, while the line widths are mostly affected by the central, fast rotating component, if there is a disk/torus.

Yet another possible but less likely effect leading to the underestimation of gas masses can also be considered. The adopted fractional abundance (10^{-9}) in the derivation of gas masses is an enhanced value found in MSFRs (Su et al. 2009) compared to that found in dark clouds. If the fractional abundance is lowered by an order of magnitude, the gas mass will increase by the same factor, consequently the discrepancy between gas masses and virial masses will be reduced to less than an order of magnitude. Under such circumstances, the scenario of CH_3CN being an outflow tracer is less favored. Nevertheless, the low fractional abundance is also unlikely given the relatively high temperatures (median $\sim$87 K) of our sample.

Spectra with higher signal-to-noise ratios may afford us the opportunity to identify the contributor of the broad CH_3CN line widths and the derived large virial masses. By analyzing the line intensities and ratios on a velocity-to-velocity basis, we will be able to estimate the gas temperature and source size for the low- and high-velocity components, and determine whether they trace predominantly a single, uniform component. Alternatively, imaging experiments with subarcsecond resolution, such as those mentioned in Section 5.3, are as desirable to clarify these scenarios directly, and to characterize the origin and the physical structure of the CH_3CN gas associated with the EGOs.

5.6. Carbon-12 to Carbon-13 Ratio

Among the sources with detections of both CH_3CN and $CH_3^{13}CN$ isotopologues, the $^{12}C/^{13}C$ ratios (or CH_3CN and

Table 5
Derived Parameters of Sources with CH$_3$CN Detection

Object	FWHM (km s^{-1})	CH$_3$CN Filling Factor[a]	CH$_3$CN N (cm^{-2})	CH$_3$CN T (K)	CH$_3$CN τ_0[b]	CH$_3^{13}$CN N (cm^{-2})	Size[c] (pc)	Molecular Gas Mass[d] ($M_\odot$)	Molecular Gas Density (cm^{-3})	Virial Mass[d] (100 $M_\odot$)
G10.34–0.14	7.9 ± 0.5	(2.3 ± 0.9) × 10^{-3}	(2.0 ± 0.9) × 10^{15}	81 ± 9	0.45	...	0.02	7.8 ± 4.7	7.9 × 10^7	4.6 ± 1.1
G11.92–AK[e]	4.8 ± 0.7	(4.9 ± 34) × 10^{-3}	(1.6 ± 12) × 10^{14}	42 ± 13	0.15	...	0.04	4.7	2.3 × 10^6	4.7[f]
G11.92–0.61	9.0 ± 0.3	(4.0 ± 0.5) × 10^{-3}	(2.0 ± 0.3) × 10^{15}	130 ± 9	0.17	(3.2 ± 0.4) × 10^{14}	0.04	48.4 ± 8.6	3.2 × 10^7	14.8 ± 1.4
G12.68–0.18	8.2 ± 0.5	(2.9 ± 0.2) × 10^{-4}	(6.3 ± 1.0) × 10^{16}	299 ± 42	0.94	(1.3 ± 0.2) × 10^{16}	0.01	171.0 ± 29.1	3.0 × 10^9	4.1 ± 0.5
G16.59–0.05	5.3 ± 0.3	(2.5 ± 0.6) × 10^{-3}	(1.6 ± 0.4) × 10^{15}	102 ± 10	0.36	(1.6 ± 0.4) × 10^{14}	0.04	32.5 ± 11.9	2.7 × 10^7	4.7 ± 0.7
G18.67+0.03[e]	9.6 ± 2.0	(2.5 ± 2.9) × 10^{-4}	(7.9 ± 11) × 10^{15}	162 ± 69	0.39	...	0.03	105.8	1.7 × 10^8	12.4 ± 8.7
G18.89–0.47	10.5 ± 1.3	1	(1.5 ± 0.1) × 10^{12}	65 ± 12	0.00	...	0.73	12.9 ± 1.1	1.3 × 10^3	372.3 ± 92.9[g]
G19.36–0.03	6.9 ± 1.0	1	(1.8 ± 0.6) × 10^{12}	135 ± 53	0.00	...	0.40	4.5 ± 1.5	2.8 × 10^3	86.6 ± 26.0[g]
G19.88–0.53	4.6 ± 0.3	(1.6 ± 0.7) × 10^{-2}	(1.0 ± 0.5) × 10^{14}	77 ± 9	0.05	(1.3 ± 0.5) × 10^{13}	0.07	7.7 ± 5.0	1.1 × 10^5	6.9 ± 1.7
G22.04+0.22	7.5 ± 0.6	(3.2 ± 0.7) × 10^{-3}	(1.0 ± 0.3) × 10^{15}	92 ± 12	0.19	(1.6 ± 0.4) × 10^{14}	0.03	17.6 ± 6.0	1.9 × 10^7	8.8 ± 1.7
G23.01–0.41	9.3 ± 0.5	(6.6 ± 0.9) × 10^{-4}	(1.6 ± 0.3) × 10^{16}	193 ± 21	0.56	(2.0 ± 0.4) × 10^{15}	0.02	95.4 ± 23.8	5.0 × 10^8	7.9 ± 1.0
G23.96–0.11	5.9 ± 0.7	(3.3 ± 0.9) × 10^{-4}	(7.9 ± 3.6) × 10^{15}	100 ± 27	1.70	...	0.01	21.4 ± 11.4	3.8 × 10^8	2.1 ± 0.6
G24.33+0.14	5.8 ± 0.4	(9.6 ± 1.0) × 10^{-4}	(7.9 ± 1.0) × 10^{15}	138 ± 16	0.91	(2.0 ± 0.2) × 10^{15}	0.03	117.7 ± 19.7	1.6 × 10^8	4.8 ± 0.6
G25.38–0.15	4.4 ± 0.6	(1.4 ± 0.6) × 10^{-3}	(1.3 ± 1.1) × 10^{15}	37 ± 12	1.45	...	0.03	20.4 ± 19.4	2.4 × 10^7	2.8 ± 1.0
G28.83–0.25[e]	5.9 ± 0.9	(2.0 ± 7.4) × 10^{-3}	(6.3 ± 25) × 10^{14}	78 ± 22	0.20	...	0.04	13.3	1.1 × 10^7	6.0
G34.26–AK	7.8 ± 0.2	(3.9 ± 0.4) × 10^{-3}	(1.0 ± 0.1) × 10^{16}	182 ± 11	0.48	(1.3 ± 0.1) × 10^{15}	0.04	226.2 ± 32.4	1.6 × 10^8	10.5 ± 0.8[f]
G34.26+0.15	4.6 ± 0.2	1	(2.1 ± 0.1) × 10^{12}	53 ± 4	0.00	(2.1 ± 0.7) × 10^{11}	0.60	12.3 ± 4.2	2.2 × 10^3	58.8 ± 11.8[g]
G34.39–AK[e]	5.5 ± 0.4	(1.6 ± 11) × 10^{-2}	(1.6 ± 11) × 10^{14}	74 ± 10	0.08	...	14.5	1.3 × 10^6	10.6[f]	
G34.39+0.22[e]	4.2 ± 0.8	(2.5 ± 20) × 10^{-3}	(4.0 ± 33) × 10^{14}	87 ± 33	0.15	...	0.03	5.5	8.3 × 10^6	2.4
G35.03+0.35	7.3 ± 1.5	1	(1.3 ± 0.1) × 10^{12}	53 ± 15	0.00	...	0.56	6.2 ± 0.7	1.4 × 10^3	136.3 ± 54.8[g]
G40.28–AK[e]	7.9 ± 1.4	(2.0 ± 9.4) × 10^{-3}	(6.3 ± 31) × 10^{14}	82 ± 30	0.14	...	0.04	13.7	1.1 × 10^7	10.8[f]
G40.28–0.22	5.1 ± 0.3	(2.5 ± 2.0) × 10^{-3}	(1.6 ± 1.4) × 10^{15}	105 ± 12	0.35	...	0.04	43.3	2.4 × 10^7	5.1 ± 2.1
G45.47+0.05	4.2 ± 0.7	1	(8.3 ± 1.2) × 10^{11}	62 ± 21	0.00	...	0.98	12.5 ± 1.9	5.2 × 10^2	79.8 ± 26.6[g]
G49.42–AK	5.8 ± 1.5	1	(1.0 ± 4.1) × 10^{13}	10 ± 8	0.00	...	...	...	...	...

Notes.

[a] Filling factor is 1 by default if the CH$_3$CN spectrum is optically thin.

[b] Optical depth of the line center for CH$_3$CN $J = 12$–11 $K = 0$ line. For the six optically thin sources, their optical depth values are smaller than 0.005 and hence are shown as 0.00 in the table.

[c] Size estimated using kinematic distance in He et al. (2012).

[d] Error in the filling factor of the six optically thin sources is assumed to be 0 in the calculation. The mass error is not shown in the table if it exceeds the mass itself.

[e] Sources with large uncertainties in best-fit filling factor and N due to low S/N in higher K transitions. The beam-averaged column density can be calculated with $N_{\mathrm{avg}} = fN$.

[f] Assume the distance is the same as its EGO counterpart.

[g] The large virial masses are led by the default values of filling factor, which cannot be determined because of their degeneracies with the column densities.
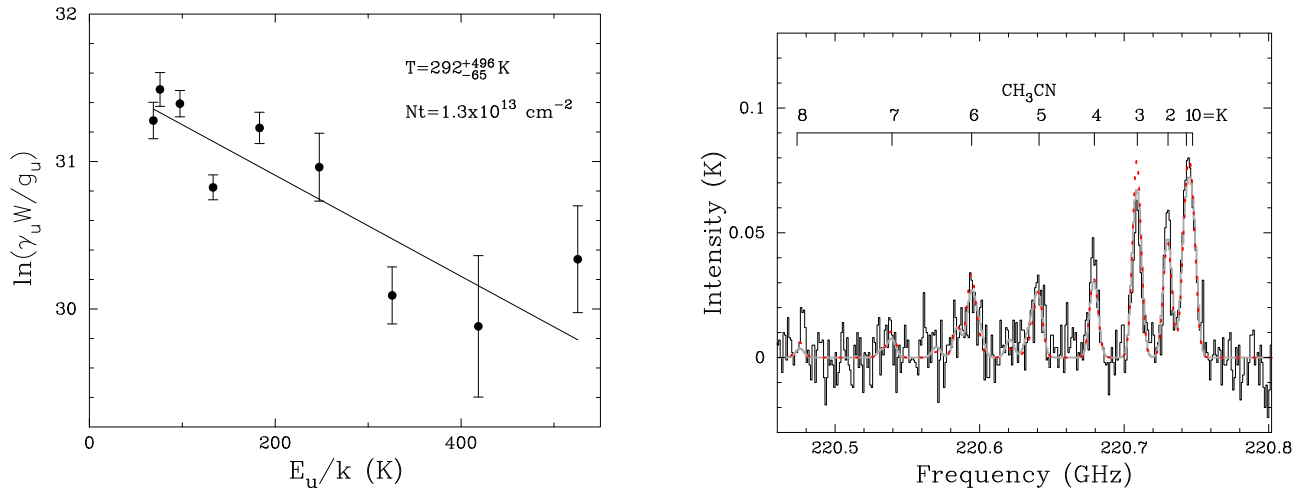
Figure 4. Left: rotation diagram of source G23.01–0.41. The best-fit temperature and column density are indicated. The $K = 3$ and $K = 6$ transitions deviate from the linear fit due to uncorrected optical depth effects. Right: the black line is the observed spectrum of G23.01–0.41 while the gray line is the best-fit result from our model. The red dotted line represents the spectrum generated by adopting parameters derived from the rotation diagram analysis.

Table 6
Comparison between FWHMs of Different Molecules

Object	CH_3CN (km s^{-1})	CH_3OH[a] (km s^{-1})	$H^{13}CO^+$[a] (km s^{-1})	HCO^+[b] (km s^{-1})	CO[b] (km s^{-1})	^{13}CO[b] (km s^{-1})	$C^{18}O$[b] (km s^{-1})
G10.34–0.14	7.95	4.58	3.66	3.87	8.33	4.58	3.28
G11.92–0.61	9.01	6.08	3.12	6.52	13.85	5.02	3.25
G12.68–0.18	8.25	2.56	2.76	⋯	⋯	⋯	⋯
G16.59–0.05	5.31	4.68	3.58	3.09	6.83	3.52	2.58
G18.67+0.03	9.60	⋯	3.58	5.02	6.85	4.32	3.5
G18.89–0.47	10.50	4.08	4	5.03	11.24	6.46	4.43
G19.36–0.03	6.87	2.18	2.5	6.37	8.9	4.56	2.72
G19.88–0.53	4.64	4.96	3.4	3.59	7.63	3.06	2.64
G22.04+0.22	7.53	6.32	2.52	2.68	8.79	4.05	2.3
G23.01–0.41	9.34	5.42	4.38	6.84	7.88	7.14	5.23
G23.96–0.11	5.86	4.1	4.24	⋯	⋯	⋯	⋯
G24.33+0.14	5.79	6.18	2.6	⋯	⋯	⋯	⋯
G25.38–0.15	4.36	4.38	3.3	5.35	12.35	5.42	3.31
G28.83–0.25	5.94	⋯	3.38	4.89	7.82	3.98	2.77
G34.26+0.15	4.58	5.1	3.72	6.8	4.26	6.93	6.88
G34.39+0.22	4.18	⋯	3.16	4.46	4.67	4.45	3.27
G35.03+0.35	7.27	6.12	5.32	4.59	7.9	3.59	3.42
G40.28–0.22	5.12	5.36	3.84	2.33	10.45	3.52	3.25
G45.47+0.05	4.19	1.84	4.84	10.92	10.97	7.33	6.51

Notes.
[a] FWHMs of $CH_3OH(4_{3,2}$–$4_{2,2})$ and $H^{13}CO^+(3$–$2)$ are from He et al. (2012).
[b] FWHMs of $HCO^+(1$–$0)$, $CO(1$–$0)$, $^{13}CO(1$–$0)$, and $C^{18}O(1$–$0)$ are from Chen et al. (2010).

$CH_3^{13}CN$ column density ratios) are estimated to be around 6. This $^{12}C/^{13}C$ ratio is significantly smaller than the interstellar value of ~60, even though measurements of the latter often exhibit large intrinsic scatter as well as variations over a range of galactocentric radii (Wilson & Rood 1994). Observationally, the low $^{12}C/^{13}C$ ratio results from $CH_3^{13}CN$ being much brighter than expected when a normal ratio is used. This is evident not only in our observed spectra, but also in other studies. For example, in Cyganowski et al. (2011b), the intensity of $CH_3^{13}CN$ lines is significantly underestimated in G11.92–0.61 when a $^{12}C/^{13}C$ ratio of 60 is enforced. Pankonin et al. (2001) had obtained a relative intensity of the $^{13}C/^{12}C$ species in the range from 0.09 to 0.32 (or equivalently 3–11 in $^{12}C/^{13}C$), which is also much smaller than the expected

$^{12}C/^{13}C$ abundance ratio. They attributed it to the high opacity of CH_3CN (8–25 for the $J = 12$–11, $K = 2$ component) in the sources with $CH_3^{13}CN$ detection. In our line profile analysis, the effect of optical depth has been taken into account, although the "overbright" $CH_3^{13}CN$ still cannot be accounted for. We have attempted to modify our line-profile fitting analysis by relieving the requirement of a Gaussian profile, but taking the integrated intensity on an individual velocity/channel basis for every K component. Still, the intensity ratios between the K components prevented the column densities and hence optical depths from reaching satisfactory values to accommodate the observed $CH_3^{13}CN$ intensities. It is noticeable, however, that our sources with $CH_3^{13}CN$ detection have higher temperatures and higher CH_3CN column densities. It is possible that the
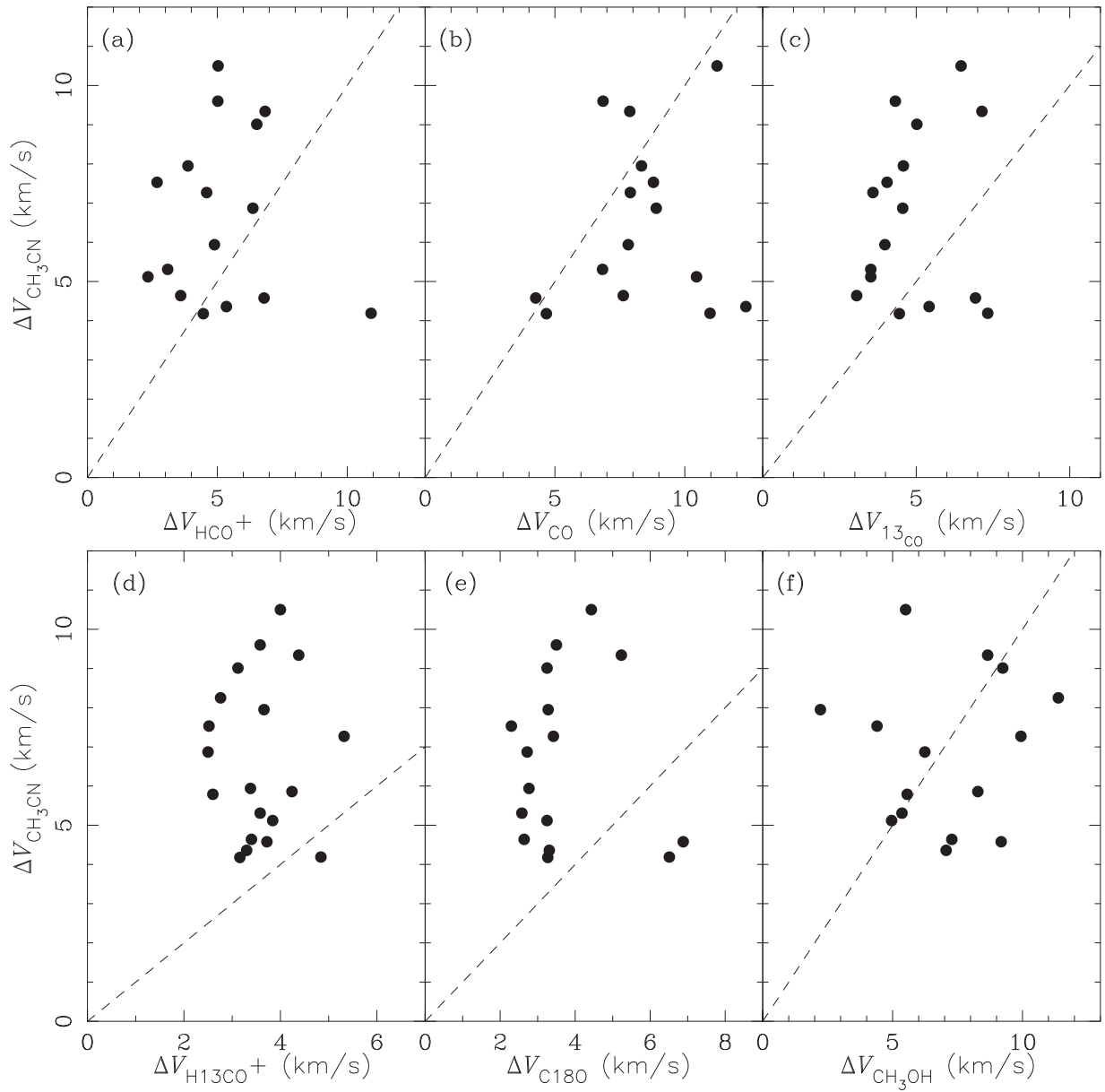
Figure 5. Comparisons of FWHM line widths of CH_3CN with (a) $HCO^+(1–0)$, (b) $H^{13}CO^+(3–2)$, (c) $CO(1–0)$, (d) $^{13}CO(1–0)$, (e) $C^{18}O(1–0)$, (f) $CH_3OH(4_{3,2}–4_{2,2})$.

simple and generic line fitting model used in the past is still underestimating the optical depth of CH_3CN. A more sophisticated source model and radiative transfer scheme may be needed for a better determination and to confirm whether the $^{12}C/^{13}C$ ratios are exceptionally low in our EGO samples and MSFRs in general.

6. Conclusions

We observed a sample of 56 EGOs and *AKARI* bright sources with the SMT. CH_3CN $J = 12$–11 is detected toward 19 EGOs and five *AKARI* sources. The low detection rate of *AKARI* bright sources compared to that of EGOs provides weak evidence that these *AKARI* sources are physically associated with the EGOs. We found CH_3CN detection in at least 54% (19 out of 35) of EGOs. The CH_3CN column densities span the range 10^{14}–10^{17} cm^{-2}. The average FWHM in velocity is 6.7 ± 2.0 km s^{-1}. Our main conclusions are listed below.

1. The sources of CH_3CN emission are compact (~0.01–0.08 pc in size) while the gas temperatures derived from fitting CH_3CN vary from 40 to 300 K. As shown by our best-fit results, the values of filling factors fall in the range 10^{-2}–10^{-4}, which suggests a significant beam dilution effect. This may have resulted in some sources with weaker CH_3CN emission being undetected. Therefore, the detection rate should be treated as a lower limit.

2. The derived virial masses are greater than the gas masses by one to two orders of magnitude, possibly because CH_3CN is tracing energetic motions such as outflows and shocks, or because of the presence of unresolved CH_3CN emitting components. The gas masses are estimated by assuming a CH_3CN fractional abundance of 10^{-9}, while the virial masses are derived from the CH_3CN line widths assuming spherical geometry. Over-estimation in virial masses will occur if the sources in our
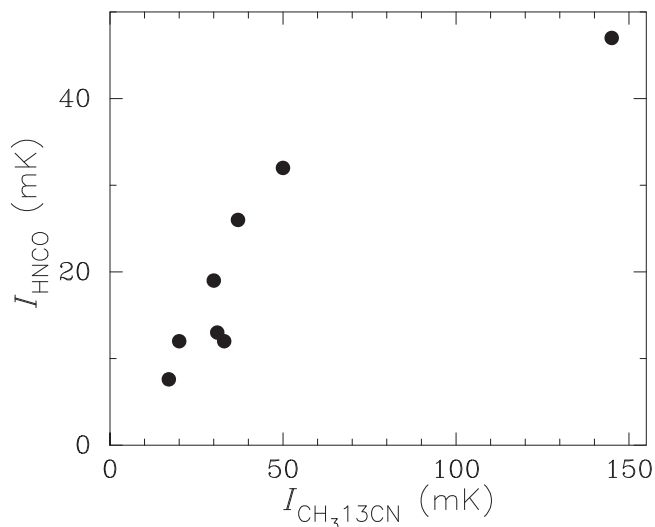
Figure 6. Peak intensity of HNCO 10(1, 9)–9(1, 8) and CH$_3$^{13}CN J = 12–11.

sample consist of multiple gas components that cannot be resolved by the SMT, which could be the virialized rotation structures around the YSOs traced by CH$_3$CN as previously observed.

3. In some sources, both CH$_3$CN and its isotopologue CH$_3$^{13}CN are detected with a strong signal and this results in a ^{12}C/^{13}C abundance ratio of $\sim$4–10. This value is much lower than the nominal interstellar value but consistent with previous studies in MSFRs; this has been attributed to the optical depth effects. Detailed radiative transfer models will be able to verify the observed abundance ratio.

ORCID iDs

T. Hung ● https://orcid.org/0000-0002-9878-7889
Sheng-Yuan Liu ● https://orcid.org/0000-0003-4603-7119
J. H. He ● https://orcid.org/0000-0002-3938-4393
Satoko Takahashi ● https://orcid.org/0000-0002-7287-4343
Huei-Ru Chen ● https://orcid.org/0000-0002-9774-1846

References

Araya, E., Hofner, P., Kurtz, S., Bronfman, L., & DeDeo, S. 2005, ApJS, 157, 279
Araya, E., Hofner, P., Sewiło, M., et al. 2007, ApJ, 669, 1050
Beltrán, M. T., Cesaroni, R., Neri, R., et al. 2005, A&A, 435, 901
Beltrán, M. T., Cesaroni, R., Neri, R., & Codella, C. 2011, A&A, 525, 151
Beltrán, M. T., & de Wit, W. J. 2016, A&ARv, 24, 6
Boucher, D., Burie, J., Bauer, A., Dubrulle, A., & Demaison, J. 1980, JPCRD, 9, 659
Brogan, C. L., Hunter, T. R., Cyganowski, C. J., et al. 2011, ApJL, 739, L16
Chen, H.-R., Welch, W. J., Wilner, D. J., & Sutton, E. C. 2006, ApJ, 639, 975
Chen, H.-R. V., Keto, E., Zhang, Q., et al. 2016, ApJ, 823, 125
Chen, X., Gan, C.-G., Ellingsen, S. P., et al. 2013, ApJS, 206, 9
Chen, X., Shen, Z.-Q., Li, J.-J., Xu, Y., & He, J.-H. 2010, ApJ, 710, 150
Codella, C., Benedettini, M., Beltrán, M. T., et al. 2009, A&A, 507, L25
Cyganowski, C. J., Brogan, C. L., Hunter, T. R., et al. 2012, ApJL, 760, L20
Cyganowski, C. J., Brogan, C. L., Hunter, T. R., & Churchwell, E. 2009, ApJ, 702, 1615
Cyganowski, C. J., Brogan, C. L., Hunter, T. R., & Churchwell, E. 2011a, ApJ, 743, 56
Cyganowski, C. J., Brogan, C. L., Hunter, T. R., Churchwell, E., & Zhang, Q. 2011b, ApJ, 729, 124
Cyganowski, C. J., Whitney, B. A., Holden, E., et al. 2008, AJ, 136, 2391
De Buizer, J. M., Radomski, J. T., Telesco, C. M., & Piña, R. K. 2003, ApJ, 598, 1127
De Buizer, J. M., & Vacca, W. D. 2010, AJ, 140, 196
Doi, Y., Etxaluze Azkonaga, M., White, G., et al. 2009, in SPICA Joint European/Japanese Workshop, ed. A. M. Heras et al. (Les Ulis: EDP Sciences), 04018
Ellingsen, S. P. 2006, ApJ, 638, 241
Ge, J. X., He, J. H., Chen, X., & Takahashi, S. 2014, MNRAS, 445, 1170
Goldsmith, P. F., & Langer, W. D. 1999, ApJ, 517, 209
He, J. H., Takahashi, S., & Chen, X. 2012, ApJS, 202, 1
Hernández-Hernández, V., Zapata, L., Kurtz, S., & Garay, G. 2014, ApJ, 786, 38
Ilee, J. D., Cyganowski, C. J., Nazari, P., et al. 2016, MNRAS, 462, 4386
Johnston, K. G., Robitaille, T. P., Beuther, H., et al. 2015, ApJL, 813, L19
Kurtz, S., Hofner, P., & Álvarez, C. V. 2004, ApJS, 155, 149
Lee, H.-T., Takami, M., Duan, H.-Y., et al. 2012, ApJS, 200, 2
Leurini, S., Codella, C., Zapata, L., et al. 2011, A&A, 530, A12
Loren, R. B., & Mundy, L. G. 1984, ApJ, 286, 232
Maud, L. T., Cesaroni, R., Kumar, M. S. N., et al. 2018, A&A, 620, A31
Millar, T. J., MacDonald, G. H., & Gibb, A. G. 1997, A&A, 325, 1163
Minh, Y. C., Liu, H. B., & Galván-Madrid, R. 2016, ApJ, 824, 99
Minier, V., Ellingsen, S. P., Norris, R. P., & Booth, R. S. 2003, A&A, 403, 1095
Noriega-Crespo, A., Morris, P., Marleau, F. R., et al. 2004, ApJS, 154, 352
Oyabu, S., Yamamura, I., Alfageme, C., et al. 2010, Proc. SPIE, 7731, 77312P
Pankonin, V., Churchwell, E., Watson, C., & Bieging, J. H. 2001, ApJ, 558, 194
Purcell, C. R., Balasubramanyam, R., Burton, M. G., et al. 2006, MNRAS, 367, 553
Qiu, K., Zhang, Q., Megeath, S. T., et al. 2008, ApJ, 685, 1005
Rathborne, J. M., Jackson, J. M., Chambers, E. T., et al. 2005, ApJL, 630, L181
Rathborne, J. M., Jackson, J. M., & Simon, R. 2006, ApJ, 641, 389
Rathborne, J. M., Simon, R., & Jackson, J. M. 2007, ApJ, 662, 1082
Reach, W. T., Rho, J., Tappe, A., et al. 2006, AJ, 131, 1479
Rodríguez-Fernández, N. J., Tafalla, M., Gueth, F., & Bachiller, R. 2010, A&A, 516, A98
Rosero, V., Hofner, P., Kurtz, S., Bieging, J., & Araya, E. D. 2013, ApJS, 207, 12
Sanna, A., Moscadelli, L., Cesaroni, R., et al. 2010a, A&A, 517, 71
Sanna, A., Moscadelli, L., Cesaroni, R., et al. 2010b, A&A, 517, 78
Shepherd, D. S., Povich, M. S., Whitney, B. A., et al. 2007, ApJ, 669, 464
Smith, H. A., Hora, J. L., Marengo, M., & Pipher, J. L. 2006, ApJ, 645, 1264
Su, Y.-N., Liu, S.-Y., Wang, K.-S., Chen, Y.-H., & Chen, H.-R. 2009, ApJL, 704, L5
Takami, M., Chen, H.-H., Karr, J. L., et al. 2012, ApJ, 748, 8
van Dishoeck, E. F., & Blake, G. A. 1998, ARA&A, 36, 317
Wang, K.-S., Kuan, Y.-J., Liu, S.-Y., & Charnley, S. B. 2010, ApJ, 713, 1192
Wilner, D. J., Ho, P. T. P., & Zhang, Q. 1996, AJ, 462, 339
Wilson, T. L., & Rood, R. 1994, ARA&A, 32, 191
Wink, J. E., Duvert, G., Guilloteau, S., et al. 1994, A&A, 281, 505
Wyrowski, F., Hofner, P., Schilke, P., et al. 1997, A&A, 320, L17